COPERNICUS SPACE COMPONENT SENTINEL OPTICAL IMAGING

MISSION PERFORMANCE CLUSTER SERVICE

Data Quality Report

Sentinel-3 SLSTR - August 2023

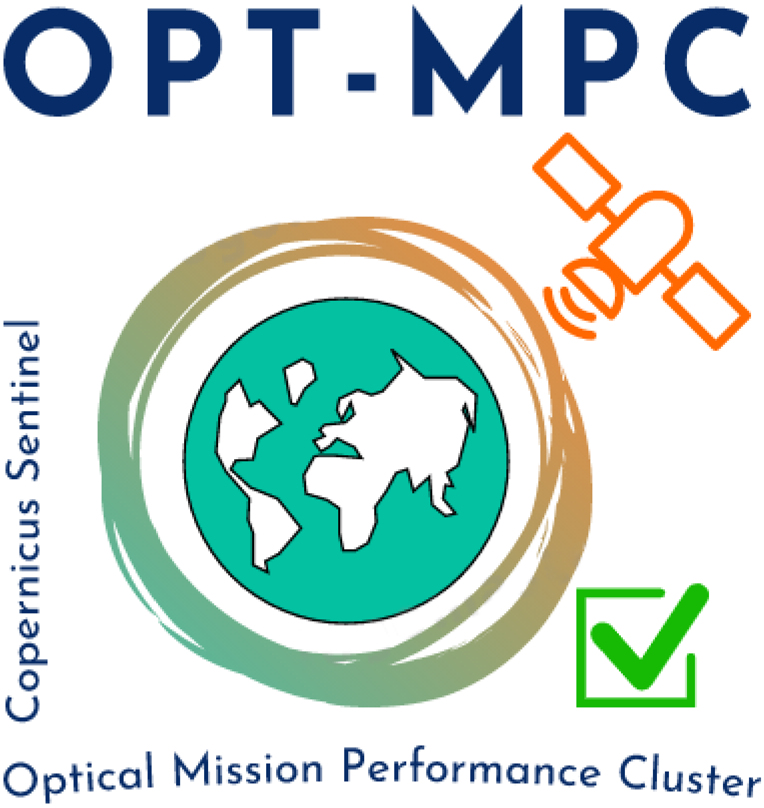

Ref.: OMPC.LDO.DQR.04.08-2023
Issue: 1.0
Date: 11/09/2023
Contract: 4000136252/21/I-BG

Customer:	ESA	**Document Ref.:**	OMPC.LDO.DQR.04.08-2023
Contract No.:	4000136252/21/I-BG	**Date:**	11/09/2023
		Issue:	1.0

Project:	COPERNICUS SPACE COMPONENT SENTINEL OPTICAL IMAGING MISSION PERFORMANCE CLUSTER SERVICE		
Title:	Data Quality Report - SLSTR - August 2023		
Author(s):	SLSTR ESL team		
Approved by:	P. Paolino, OPT-MPC SLSTR ESL Coordinator	**Authorized by**	C. Henocq, OPT-MPC S3 Technical Manager
Distribution:	ESA, EUMETSAT, published in Sentinel Online		
Accepted by ESA	S. Dransfeld, ESA TO		
Filename	OMPC.LDO.DQR.04.08-2023 - i1r0 - SLSTR Data Quality Report August 2023.docx		

Changes Log

Version	Date	Changes
1.0	11/09/2023	First version

Table of content

List of Figures

List of Tables

1 Executive Summary

This section provides a summary of the data quality for SLSTR-A and SLSTR-B over the month of operation.

Any relevant formal instrument data requirements are added under the subsequent section headers for reference.

Each month the data measured by SLSTR-A and SLSTR-B are checked for quality and it is determined whether they meet the requirements specified in Sentinel-3 Mission Requirements Document, using the methods in the Sentinel-3 Cal-Val Plan.

A summary of the status from each check performed is provided below. A traffic light system is used, where the categories are determined as follows

- Gray indicates no change over the reporting period
- Green indicates that aspect is performing optimally
- Amber indicates there are some issues noted that may affect data quality or availability this month, or a user correction that needs to be applied
- Red indicates a significant quality issue, or instrument anomaly for some of the month

Follow the link on each topic header for more detailed information contained in this document.

Topic	Instrument	Comments
Processing Baseline Version	S3A	Following a PUG issue detected on STC timeliness, a corrected version (PB 3.24 – PUG v3.49) has been delivered and deployed on 16/08/2023
	S3B	Following a PUG issue detected on STC timeliness, a corrected version (PB 3.24 – PUG v3.49) has been delivered and deployed on 17/08/2023
Event	S3A	Several events occurred this month without impact on data quality Including a decontamination phase triggered on 06-07/08
	S3B	Several events occurred this month without impact on data quality Including a power cycle phase triggered on 16-17/08
Instrument status	S3A	
	S3B	
Level-1 TIR Radiometric Validation	S3A	
	S3B	
Level-1 VIS SWIR Radiometric Validation	S3A	Vicarious validation indicates calibration offsets need to be applied to the VIS/SWIR channels New validation results using PICS method
	S3B	Vicarious validation indicates calibration offsets need to be applied to the VIS/SWIR channels New validation results using PICS method

Topic	Instrument	Comments
Level-1 Geometric Validation	S3A	
	S3B	
Level-2 LST Validation	S3A	
	S3B	
Level-2 FRP Validation	S3A	
	S3B	

2 Processing status

2.1 Processing baseline status

The Processing Baseline Version allows traceability of any changes to the software used to process the SLSTR products, and any updates to the auxiliary data files used to generate them.

The processing baseline identifier is now provided in the manifest file and in the global attributes of each file. The identifier comprises of seven characters (e.g. SL__L1_) which indicates the product type, and seven characters to indicate its version, xxx.yy.zz (e.g. 004.04.00). The version number, xxx indicates baseline collection, yy indicates change due to the IPF or ADF and zz indicates change in system components (e.g. L0, PUG) that do not impact data quality but are included to allow full traceability.

Following an issue raised on STC timelines after the deployment of PB 3.23, several corrections have been implemented on PUG 3.49 and delivered on 8th August 2023. This PB 3.24 has deployed on both S3A and S3B processing centers this month and included only corrections on the PUG.

The deployed processing baseline and IPF versions are consistent with the latest delivered versions.

IPF	IPF / Processing Baseline version	Date of deployment
S3A		
SL1	06.21 / SL__L1_.004.06.00	25/07/2023
SL2 LST	06.21 / SL__LST.004.08.02	25/07/2023
SL2 FRP (NTC)	01.08 / FRP_NTC.004.08.02	25/07/2023

IPF	IPF / Processing Baseline version	Date of deployment
S3B		
SL1	06.21 / SL__L1_.004.06.00	18/07/2023
SL2 LST	06.21 / SL__LST.004.08.02	18/07/2023
SL2 FRP (NTC)	01.08 / FRP_NTC.004.08.02	18/07/2023

Deployment of the latest S3 PB 3.24 has been done this month.
The Processing Baselines of S3A and S3B are aligned with the latest processing baseline version.

2.2 Processing anomalies

No specific issue or evolutions has been identified this month on SLSTR.

There has been no major anomaly on data quality within the reported period.

3 Events and instrument anomalies

Any events that have occurred in this month that cause significant data gaps and impact on quality are reported here.

Some background to the typical events that might occur are provided below

- **RFI Radio Frequency Interference** occurs when another satellite causes the data downlink to the receiving station to be interrupted, and the data is lost.
- **Scheduled manoeuvres** may take place for Lunar views for calibration purposes, collision avoidance, or to maintain the nominal orbit. Will often result in the pointing flag being raised, and the geolocation accuracy is not nominal during this time.
- **Blackbody cross over tests** occur approximately once per year and the hot and cold blackbodies are swapped round for instrument testing.
- **De-icing** occurs when the instrument is heated to remove the build-up of ice.

3.1 SLSTR-A

SLSTR-A was switched on and operating nominally during August 2023, with Scan Unit Electronics (SUE) scanning and autonomous switching between day and night modes, except for the following events.

In particular, at 13:08:31 UTC the 06/08/2023, S3A SLSTR experienced a **CDE Double Bit Flip anomaly and entered CDE STBY REFUSE mode**. The spacecraft was flying through the SAA at the time.

The SLSTR decontamination was started at 00:28:17.

- 06th August 12:14:10 – 07/08/2023 20:10:55 – Data gap due to decontamination period
- 10th August, 12:16:24 – 12:25:24 – Data gaps due to RFI
- 12th August, 15:07:00 – 15:13:00 – Data gaps due to RFI
- 17th August, 07:00:08 – 07:44:07 – Pointing flags due to Out-Of-Plane Manoeuvre
- 21st August, 17:28:19 – 17:31:19 – Data gaps
- 21st August, 22:31:16 – 22:33:41 – Data gaps due to processing issues

3.2 SLSTR-B

SLSTR-B was switched on and operating nominally during August 2023, with SUE scanning and autonomous switching between day and night modes, except for the following events.

In particular, **a planned Sentinel-3B SLSTR CDE powercycle** has been executed on 16/08/2023

- 4th August, 00:29:44 – 00:38:44 and 02:45:43 – 02:48:43– Data gaps due to RFI
- 6th August, 01:03:22 – 01:12:22 – Data gaps due to RFI
- 10tH August, 15:11:30 – 15:26:30 – Pointing flag raised due to In-Plane manoeuvre.
- 10th August, 18:18:29 – 18:27:29 – L2 Data gaps due to RFI
- 10th August, 18:15:29 – 19:56:28 – Data gaps due to PUG issue
- 10th August, 20:38:28 – 21:02:28 – Data gaps, cause still under investigation.
- 11th August, 11:38:21 – 11:47:21and 19:07:18 – 19:16:18 – Data gaps due to RFI
- 16th August, 07:05:29 – 07:19:29 – Pointing flag raised due to In-Plane manoeuvre.
- 16th August, 12:37:26 – 17/08/2023, 02:47:20 – Data Gaps due to SLSTR CDE powercycle
- 20th August, 16:46:40 – 16:52:40 – data gaps due to RFI
- 22nd August, 10:42:20 – 10:48:20 – Data gaps, cause still under investigation.
- 26th August, 14:44:32 – 14:53:32 – Data gaps due to RFI

4 Instrument Status

The health of the instrument impacts the data quality. This section contains in depth analysis of several instrument parameters over the month of operation, and in some cases, the latest annual and mission tends for context.

SLSTR is a scanning radiometer, and uses two black bodies for thermal calibration, and a VISCAL unit for visible and shortwave IR calibration via the Sun. The key instrument properties that are monitored include:

- instrument temperature of the baffles
- instrument temperature of the Optical Mechanical Enclosure (optical bench, flip mirror and scan mirror, internal baffles)
- detector temperatures
- scanner and flip mirror performance

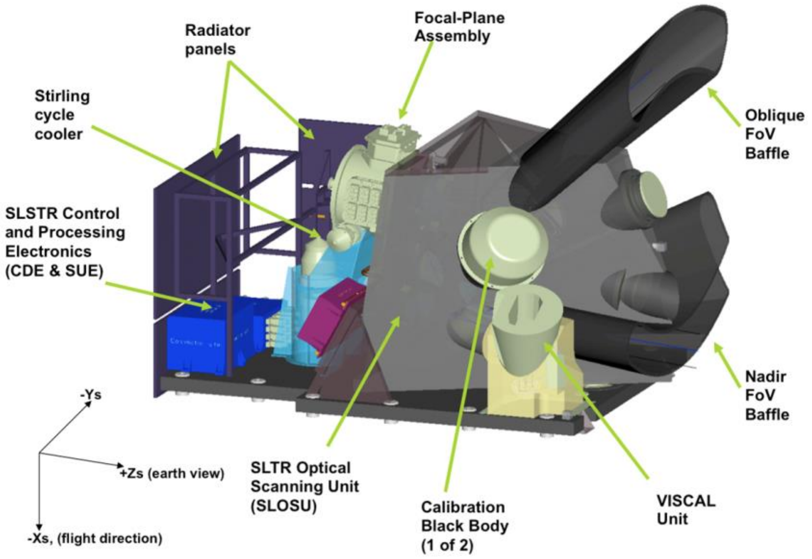

Sentinel 3 A

- Following a SLSTR CDE Double Bit Flip anomaly on S3A at 13:08:31 on 06/08/2023 ➔ SLSTR power cycle and decontamination performed to recover the instrument.
- Data gaps were present for 2 days

Sentinel 3 B

- Following the observation of a continuous EDAC counter increase and wrap around on S3B, S3 operations decides to perform a power cycle without the contamination on S3B.
- Data gaps were present for 2 days

4.1 Instrument temperatures

As a thermal infrared instrument, thermal stability and uniformity of the optical mechanical enclosure (OME) is critical to the radiometric calibration. In this section we show the orbital average temperature of the OME and instrument baffles during the month. We expect to see a very small daily variation in temperature superimposed on a stable level over the month.

4.1.1 SLSTR-A

Figure 1 shows the orbital average temperature of the OME and instrument baffles for SLSTR-A during the month.

OME Temperature over the last month	Baffle Temperature over the last month
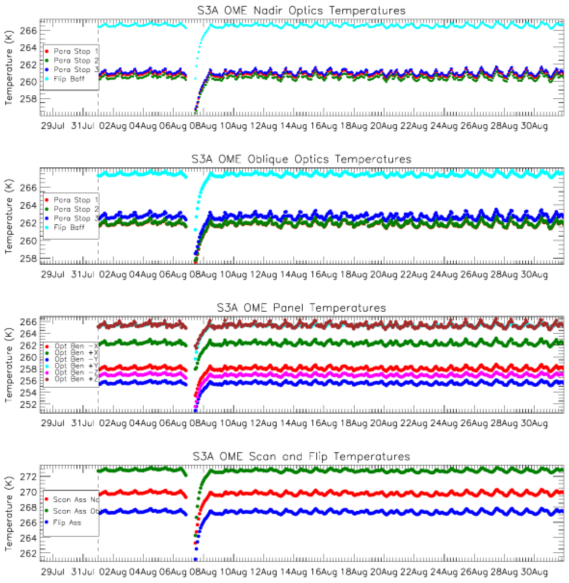	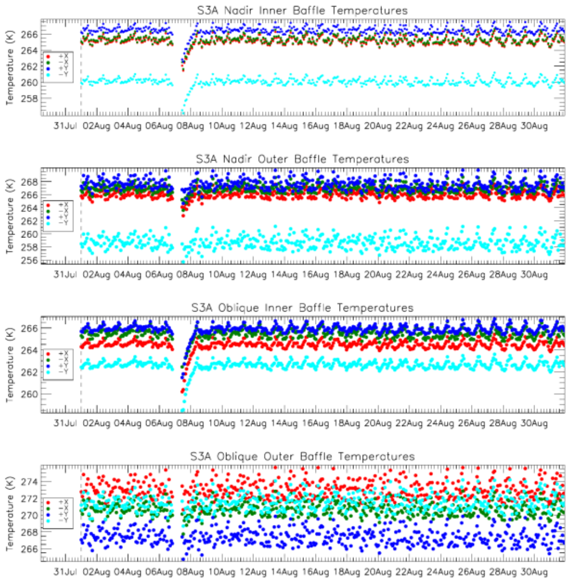

Figure 1: OME temperature trends for SLSTR-A (left) and Baffle temperature trends (right) during August 2023. The OME plot shows the three paraboloid stops and flip baffle (top two plots) and optical bench at different positions (third plots), and scanner and flip assembly (bottom plots). The Baffle plot shows the temperature at different positions on the inner and outer baffles. Each dot represents the average temperature in one orbit.

4.1.2 SLSTR-B

Figure 2 shows the orbital average temperature of the OME and instrument baffles for SLSTR-B during the month. The temperatures were stable (on top of a daily variation cycle).

OME Temperature over the last month	Baffle Temperature over the last month
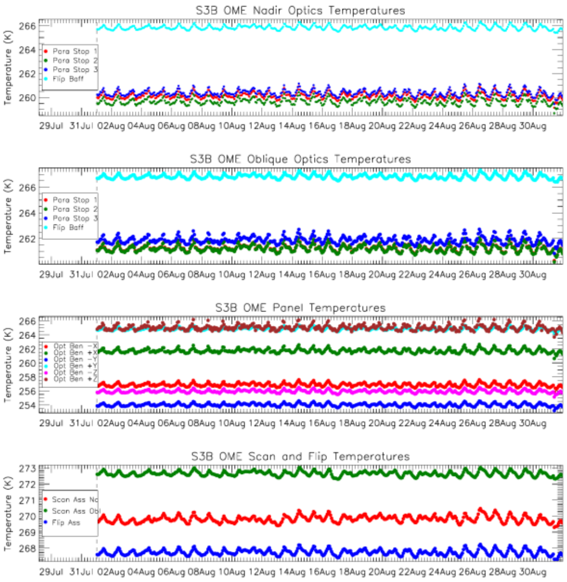	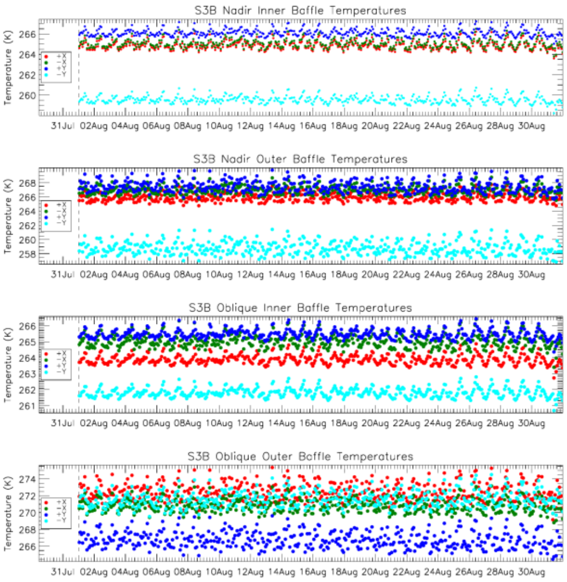

Figure 2: SLSTR-B OME temperature trends (left) and Baffle temperature trends (right) during August 2023. The OME plot shows the three paraboloid stops and flip baffle (top two plots) and optical bench at different positions (third plots), and scanner and flip assembly (bottom plots). The Baffle plot shows the temperature at different positions on the inner and outer baffles. Each dot represents the average temperature in one orbit.

4.2 Detector temperatures

The detector temperatures for both SLSTR-A and SLSTR-B were stable at their expected values over the month.

4.2.1 SLSTR-A

Figure 3 shows the annual trend in SLSTR-A detector temperatures for the past year. The temperatures from this month are consistent with the yearly trend.

Detector Temperatures over the last year

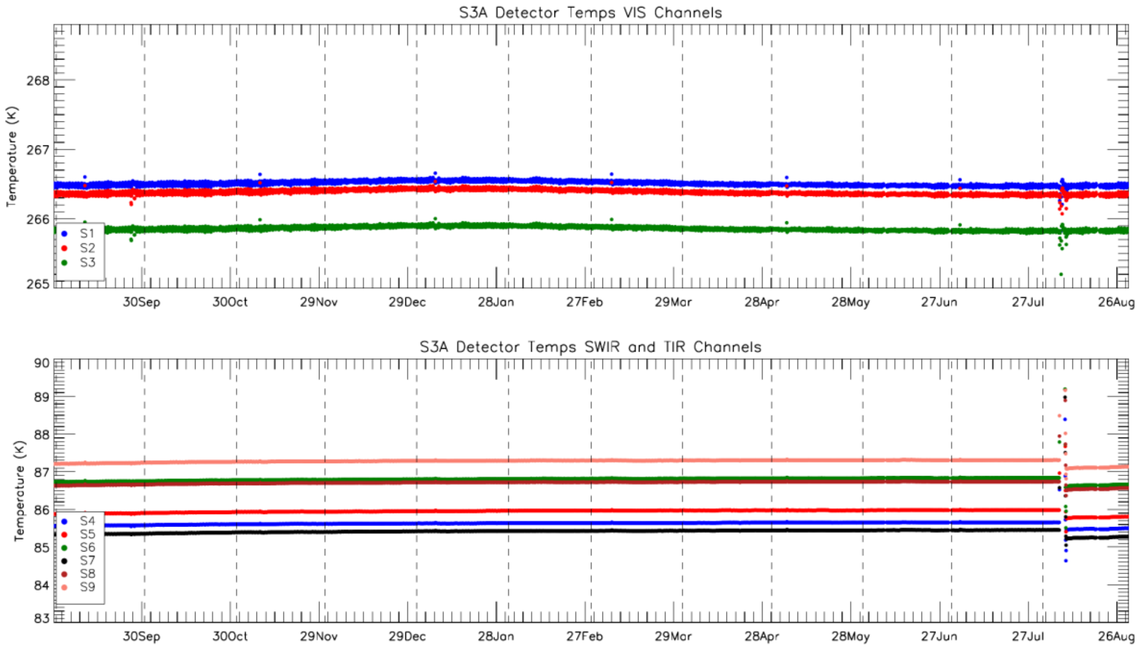

Figure 3: SLSTR-A detector temperatures for each channel for the last month of operations. The vertical dashed lines indicate the start of each month. Each dot represents the average temperature in one orbit. The different colours indicate different detectors.

4.2.2 SLSTR-B

Figure 4 shows the annual trend in SLSTR-B detector temperatures for the past year. The temperatures from this month are consistent with the yearly trend.

Detector Temperatures over the last year

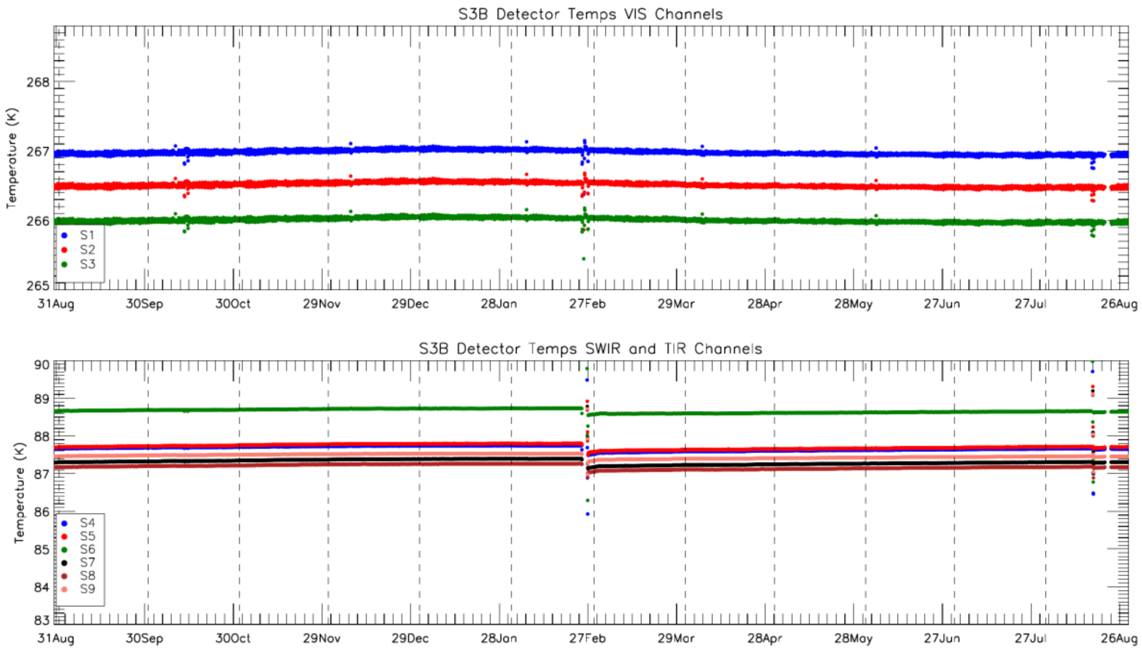

Figure 4: SLSTR-B detector temperatures for each channel for the last month of operations. The vertical dashed lines indicate the start of each month. Each dot represents the average temperature in one orbit. The different colours indicate different detectors.

4.3 Scanner performance

The actual position of the scan and flip mirrors is measured by the instrument, and in this section we show the statistics of the difference from the expected linear control law for each mirror in each view during August 2023. The performance has been consistent with previous operations and does not appear to be degrading. For reference, one arcsecond corresponds to roughly 4 m on the ground.

4.3.1 SLSTR-A

Figure 5 shows the statistics of the difference from the expected linear control law for each mirror in each view for SLSTR-A during August 2023.

Nadir view scanner and flip jitter	**Oblique view scanner and flip jitter**

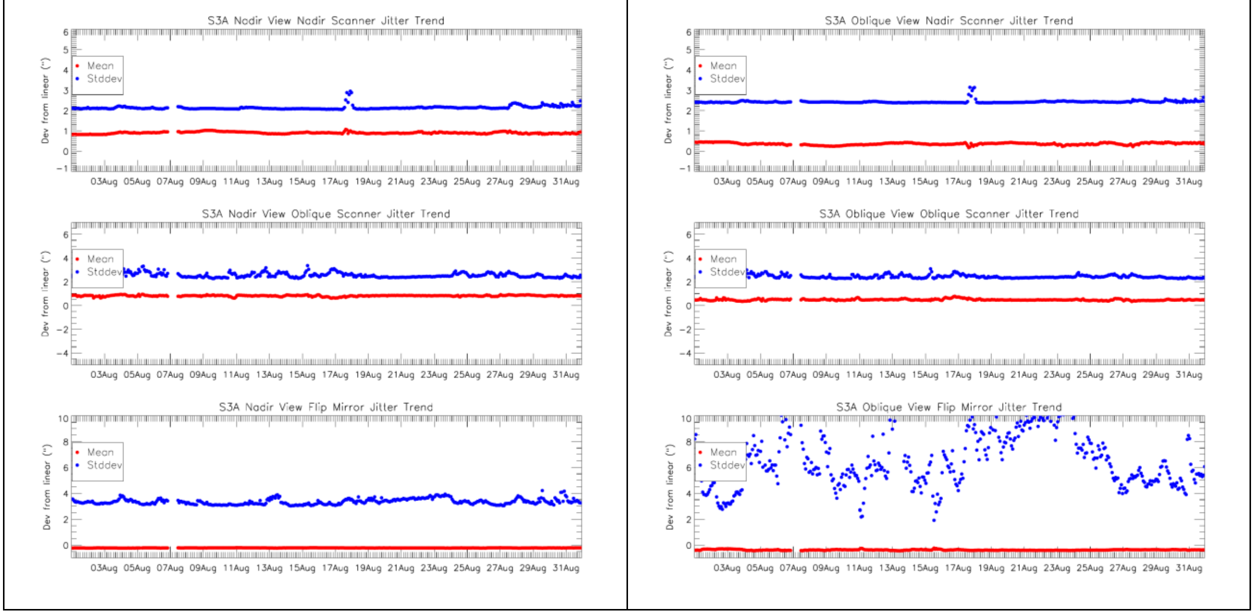

Figure 5: SLSTR-A scanner and flip jitter for August 2023, showing mean and stddev from expected position per orbit (red and blue respectively) for the nadir view (left) and oblique view (right). The plots show the nadir scanner (top), oblique scanner (middle) and flip mirror (bottom).

4.3.2 SLSTR-B

Figure 6 shows the statistics of the difference from the expected linear control law for each mirror in each view for SLSTR-B during August 2023.

Nadir view scanner and flip jitter	Oblique view scanner and flip jitter
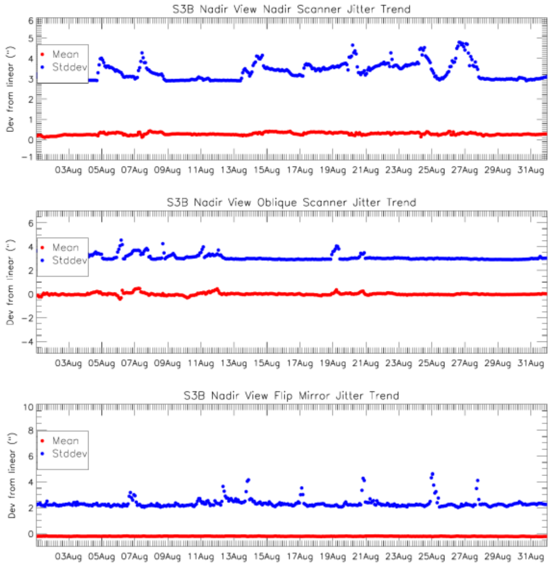	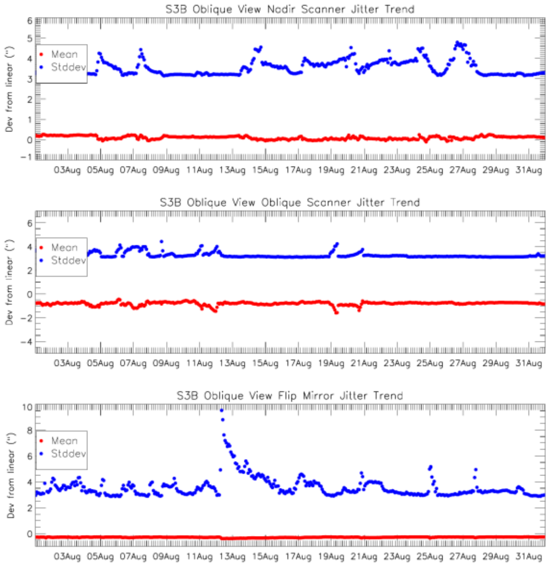

Figure 6: SLSTR-B scanner and flip jitter for August 2023, showing mean and stddev difference from expected position per orbit (red and blue respectively) for the nadir view (left) and oblique view (right). The plots show the nadir scanner (top), oblique scanner (middle) and flip mirror (bottom).

4.4 Black-Bodies

The monthly orbital average blackbody temperatures are shown in this section. The temperatures were stable on top of a daily variation cycle. There are also longer term trends which show a yearly variation, with temperatures rising as the Earth approaches perihelion at the beginning of January – this variation is shown in the monthly averages in Figure 7 and Table 5.

Latest mission trend of +Y hot BB temperature

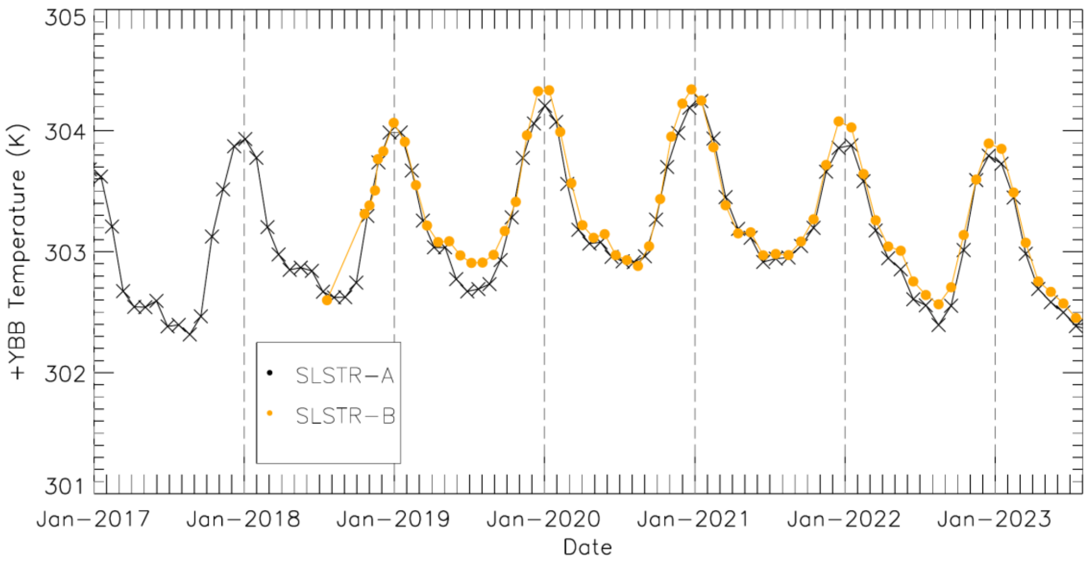

Figure 7: SLSTR-A and SLSTR-B long term trends in average +YBB temperature, showing yearly variation. The vertical dashed lines indicate the 1st January in each year.

4.4.1 SLSTR-A

The monthly orbital average blackbody temperatures for SLSTR-A are shown in Figure 8. The temperatures were stable on top of a daily variation cycle. Figure 8 also shows the gradients across the blackbody baseplate (i.e., each Platinum Resistance Thermometer (PRT) sensor reading relative to the mean). The gradients are stable and within their expected range of ±20mK.

Blackbody temperature over the month

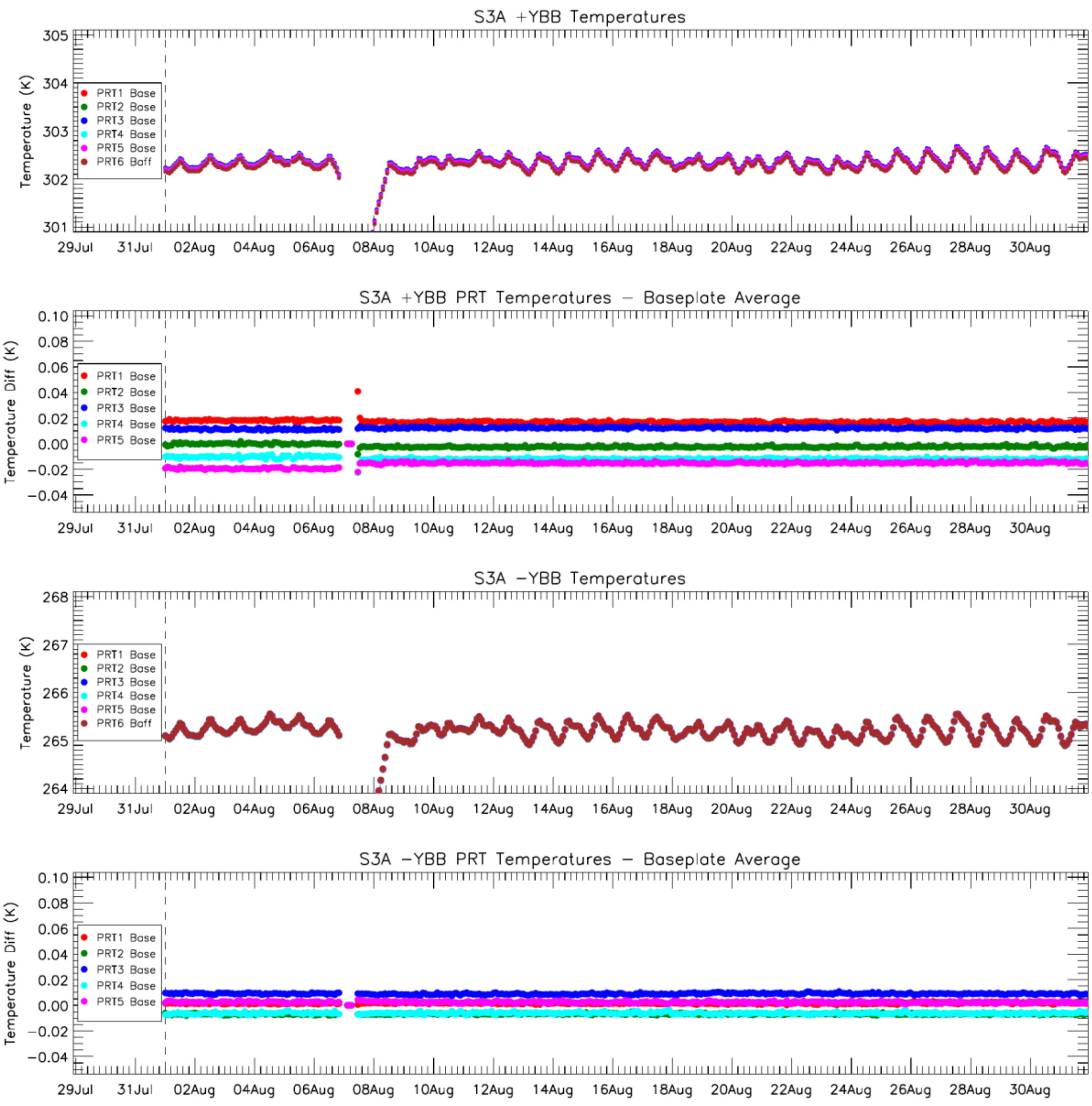

Figure 8: SLSTR-A blackbody temperature and baseplate gradient trends during August 2023 measured by different sensors at various positions in the BB and Baseplate. Each dot represents the average temperature in one orbit.

4.4.2 SLSTR-B

The monthly orbital average blackbody temperatures for SLSTR-B are shown in Figure 9. The temperatures were stable on top of a daily variation cycle. Figure 9 also shows the gradients across the blackbody baseplate (i.e., each Platinum Resistance Thermometer (PRT) sensor reading relative to the mean). The gradients are stable and within their expected range of ±20mK, except for the +Y blackbody for SLSTR-B which has a higher gradient. This higher gradient is expected and consistent with measurements made before launch.

Blackbody temperature over the month

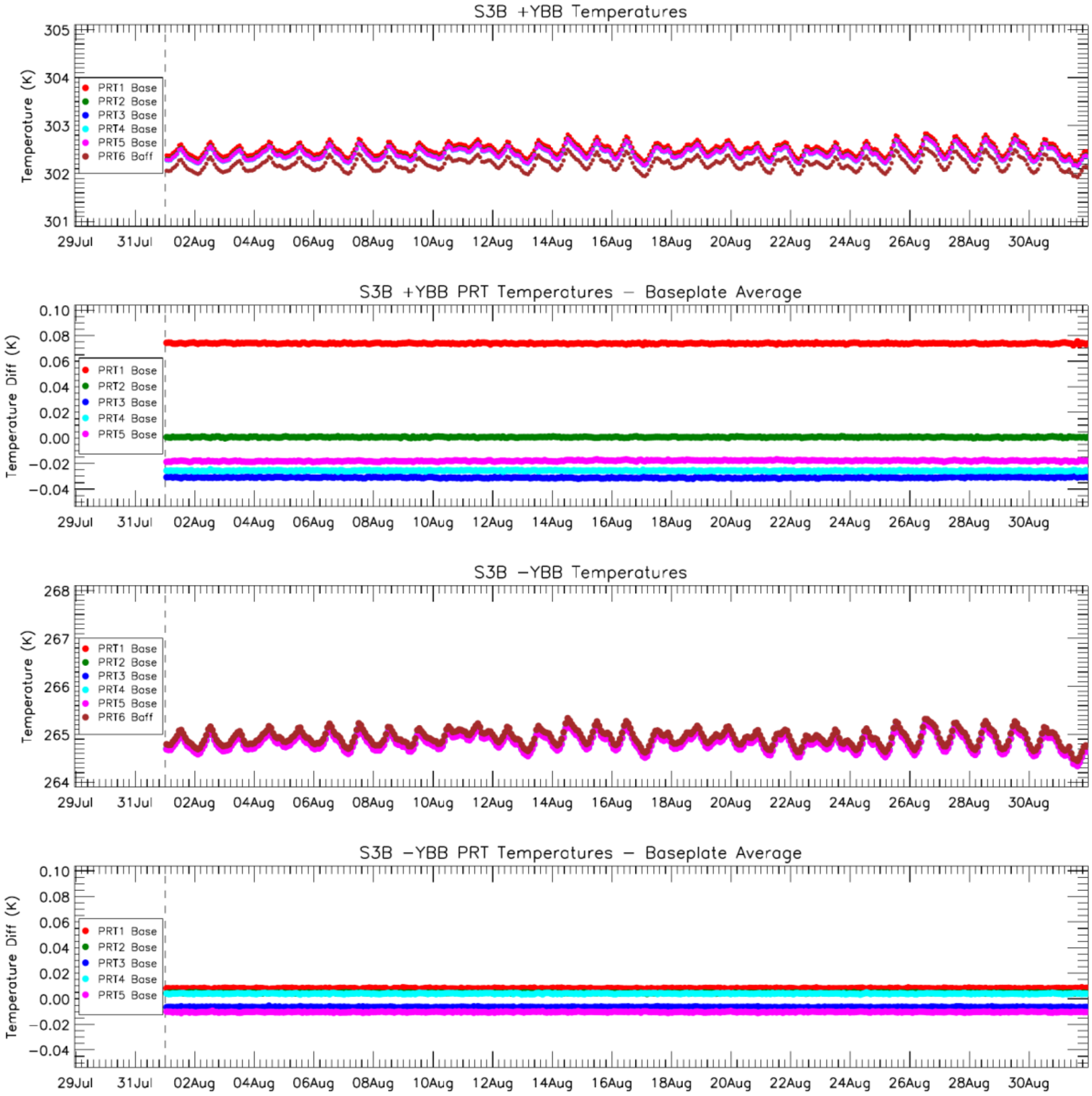

Figure 9: SLSTR-B blackbody temperature and baseplate gradient trends during August 2023 measured by different sensors at various positions in the BB and Baseplate. Each dot represents the average temperature in one orbit.

4.5 Detector noise levels

4.5.1 SLSTR-A VIS and SWIR channel signal-to-noise

The VIS and SWIR channel noise for SLSTR-A during August 2023 was stable and consistent with previous operations - the signal-to-noise ratio of the measured VISCAL signal over the past year is plotted in Figure 10 and Figure 11. Table 1 and Table 2 give the average monthly signal-to-noise (excluding the instrument decontaminations). These values average over the significant detector-detector dispersion for the SWIR channels that is shown in Figure 11. Note that these averages are now calculated for each calendar month, whereas in data quality reports before January 2022 they were aligned to the satellite 27 day repeat cycles.

Table 1: Average SLSTR-A reflectance factor, and signal-to-noise ratio of the measured VISCAL signal for the last 11 months, averaged over all detectors for the nadir view.

	Average Reflectance Factor	Nadir Signal-to-noise ratio										
		Oct 2022	Nov 2022	Dec 2022	Jan 2023	Feb 2023	Mar 2023	Apr 2023	May 2023	Jun 2023	Jul 2023	Aug 2023
S1	0.187	246	245	239	239	239	242	244	239	234	235	238
S2	0.194	245	248	246	246	243	241	243	243	242	241	242
S3	0.190	224	226	228	231	229	225	223	218	213	216	222
S4	0.191	171	172	173	174	172	171	170	166	164	164	168
S5	0.193	285	286	286	291	289	284	283	280	280	279	280
S6	0.175	183	184	186	187	185	183	181	180	178	178	181

Table 2: Average SLSTR-A reflectance factor, and signal-to-noise ratio of the measured VISCAL signal for the last 11 months, averaged over all detectors for the oblique view.

	Average Reflectance Factor	Oblique Signal-to-noise ratio										
		Oct 2022	Nov 2022	Dec 2022	Jan 2023	Feb 2023	Mar 2023	Apr 2023	May 2023	Jun 2023	Jul 2023	Aug 2023
S1	0.166	264	267	262	259	259	262	261	252	242	246	250
S2	0.170	262	269	271	268	262	260	258	255	250	256	257
S3	0.168	226	231	236	238	235	232	226	219	213	217	222
S4	0.166	139	139	140	139	138	138	138	137	134	136	138
S5	0.166	215	217	215	211	209	214	214	214	208	213	213
S6	0.155	132	133	133	131	129	131	131	131	130	129	132

VIS channels SNR over the last year

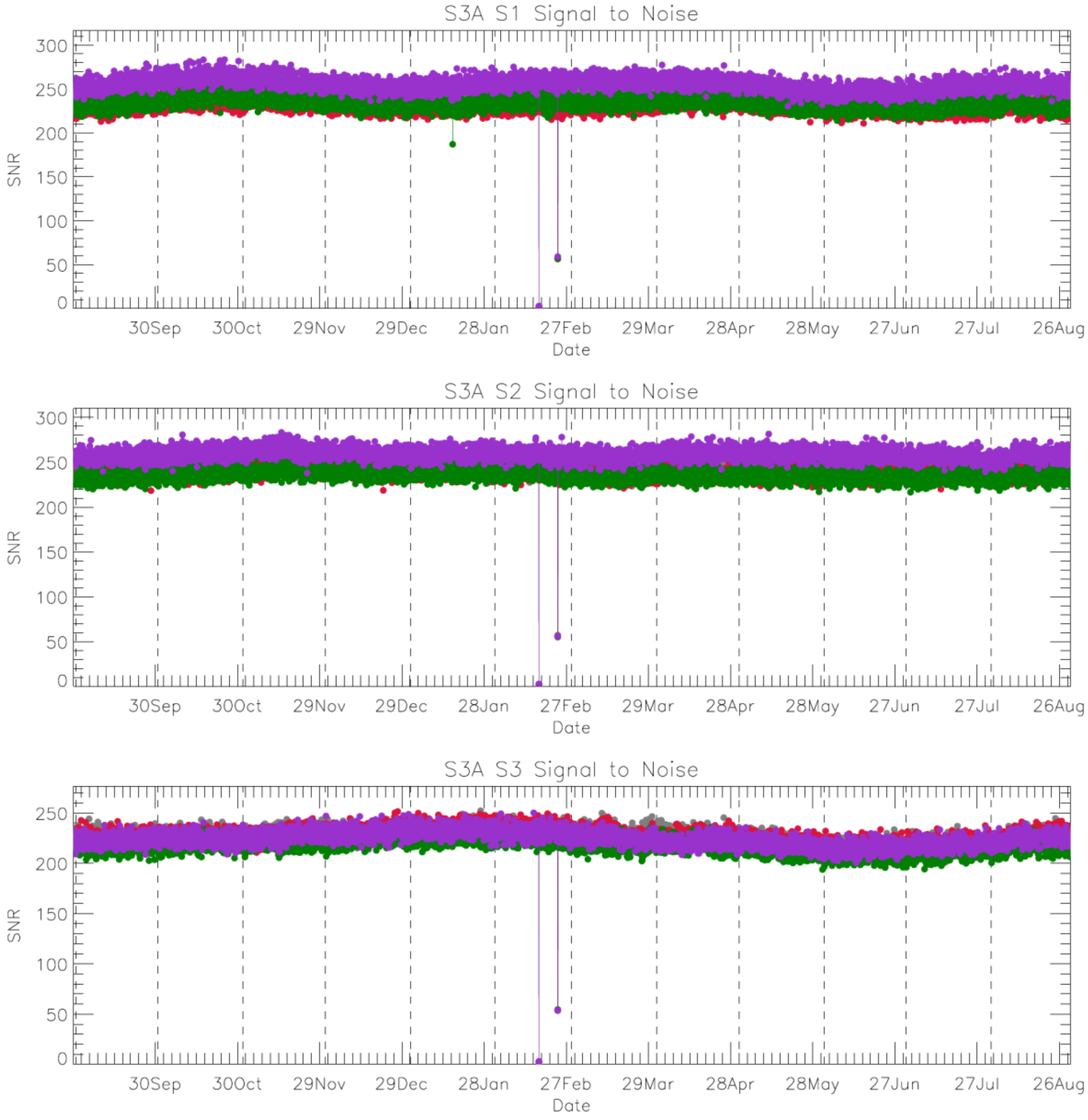

Figure 10: VIS channel signal-to-noise of the measured VISCAL signal in each orbit for the last year of operations for SLSTR-A. Different colours indicate different detectors. The vertical dashed lines indicate the start of each month.

SWIR SNR over the last year

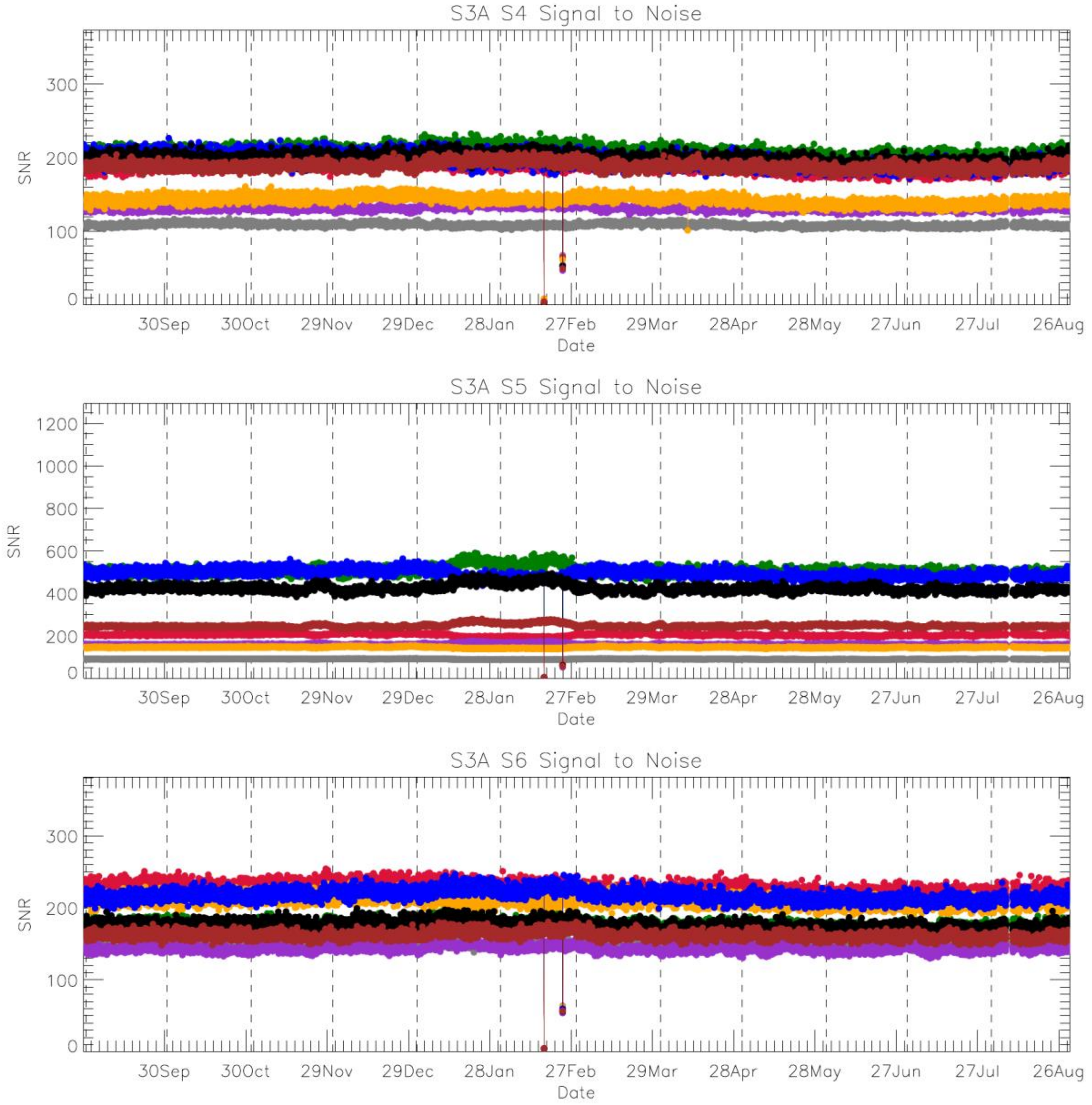

Figure 11. SWIR channel signal-to-noise of the measured VISCAL signal in each orbit for the last year of operations for SLSTR-A. Different colours indicate different detectors. The vertical dashed lines indicate the start of each month.

4.5.2 SLSTR-B VIS and SWIR channel signal-to-noise

The monthly average VIS and SWIR channel signal-to-noise ratios for SLSTR-B are shown in Table 3 and Table 4. These values average over a significant detector-detector dispersion for the SWIR channels.

Table 3: Average SLSTR-B reflectance factor, and signal-to-noise ratio of the measured VISCAL signal for the last 11 months, averaged over all detectors for the nadir view.

	Average Reflectance Factor	Nadir Signal-to-noise ratio										
		Oct 2022	**Nov 2022**	**Dec 2022**	**Jan 2023**	**Feb 2023**	**Mar 2023**	**Apr 2023**	**May 2023**	**Jun 2023**	**Jul 2023**	**Aug 2023**
S1	0.177	233	220	232	238	238	223	227	228	221	219	226
S2	0.192	218	256	223	221	221	218	215	214	216	214	215
S3	0.194	224	248	221	223	226	222	217	213	214	216	219
S4	0.186	127	129	131	131	130	129	129	128	126	126	126
S5	0.184	240	251	243	242	243	243	240	239	238	237	238
S6	0.162	157	162	163	165	165	162	161	159	159	157	159

Table 4: Average SLSTR-B reflectance factor, and signal-to-noise ratio of the measured VISCAL signal for the last 11 months, averaged over all detectors for the oblique view.

	Average Reflectance Factor	Oblique Signal-to-noise ratio										
		Oct 2022	**Nov 2022**	**Dec 2022**	**Jan 2023**	**Feb 2023**	**Mar 2023**	**Apr 2023**	**May 2023**	**Jun 2023**	**Jul 2023**	**Aug 2023**
S1	0.157	224	220	224	228	222	217	219	217	208	208	216
S2	0.168	249	256	257	256	255	251	245	245	245	241	242
S3	0.172	250	248	250	253	253	248	237	232	234	238	239
S4	0.168	129	129	133	132	131	131	130	127	124	126	126
S5	0.172	247	251	252	251	251	251	251	249	248	248	247
S6	0.152	185	187	189	188	186	188	187	182	180	180	182

VIS channels SNR over the last year

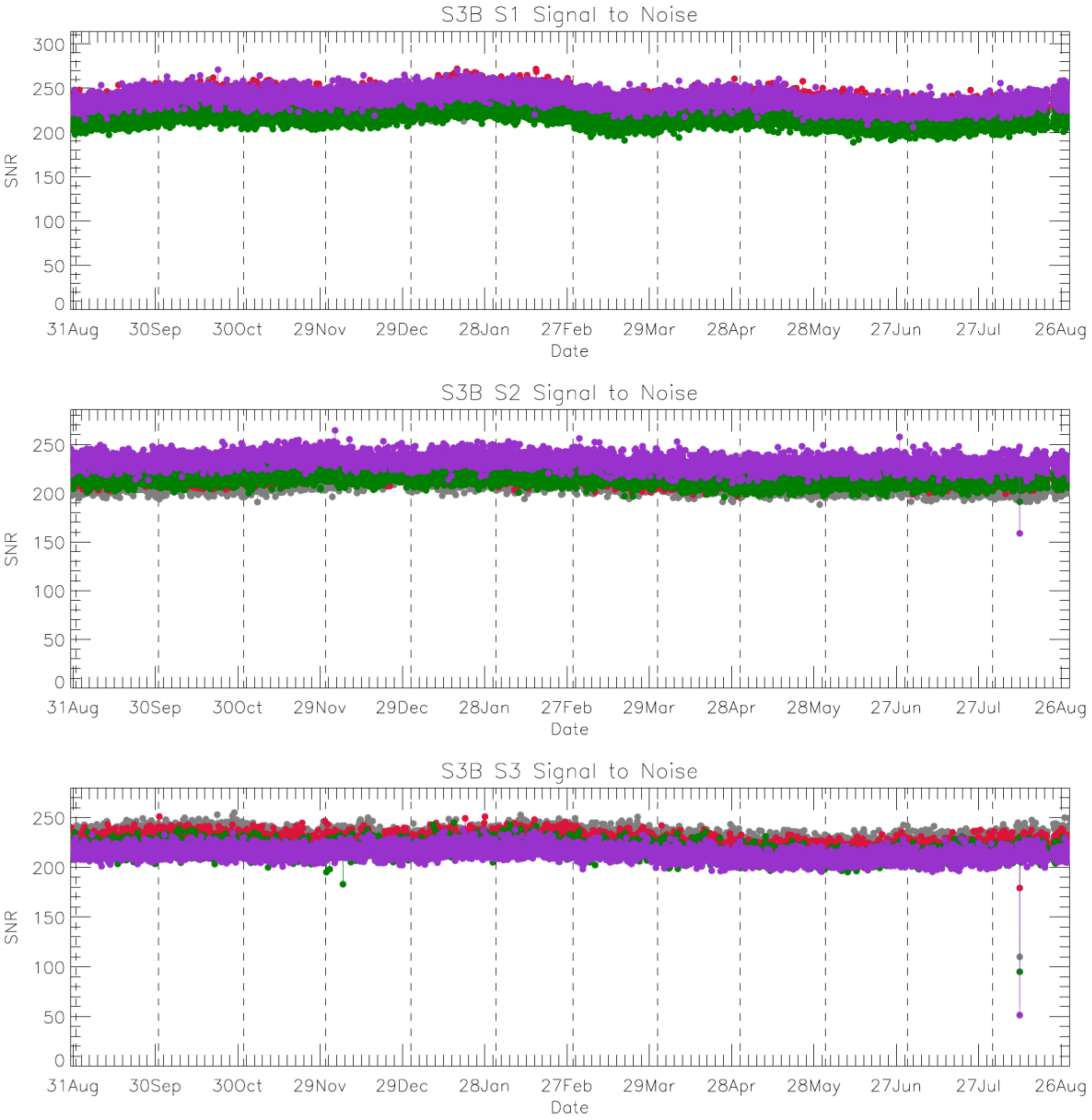

Figure 12: VIS channel signal-to-noise of the measured VISCAL signal in each orbit for the last year of operations for SLSTR-B. Different colours indicate different detectors. The vertical dashed lines indicate the start of each month.

SWIR SNR over the last year

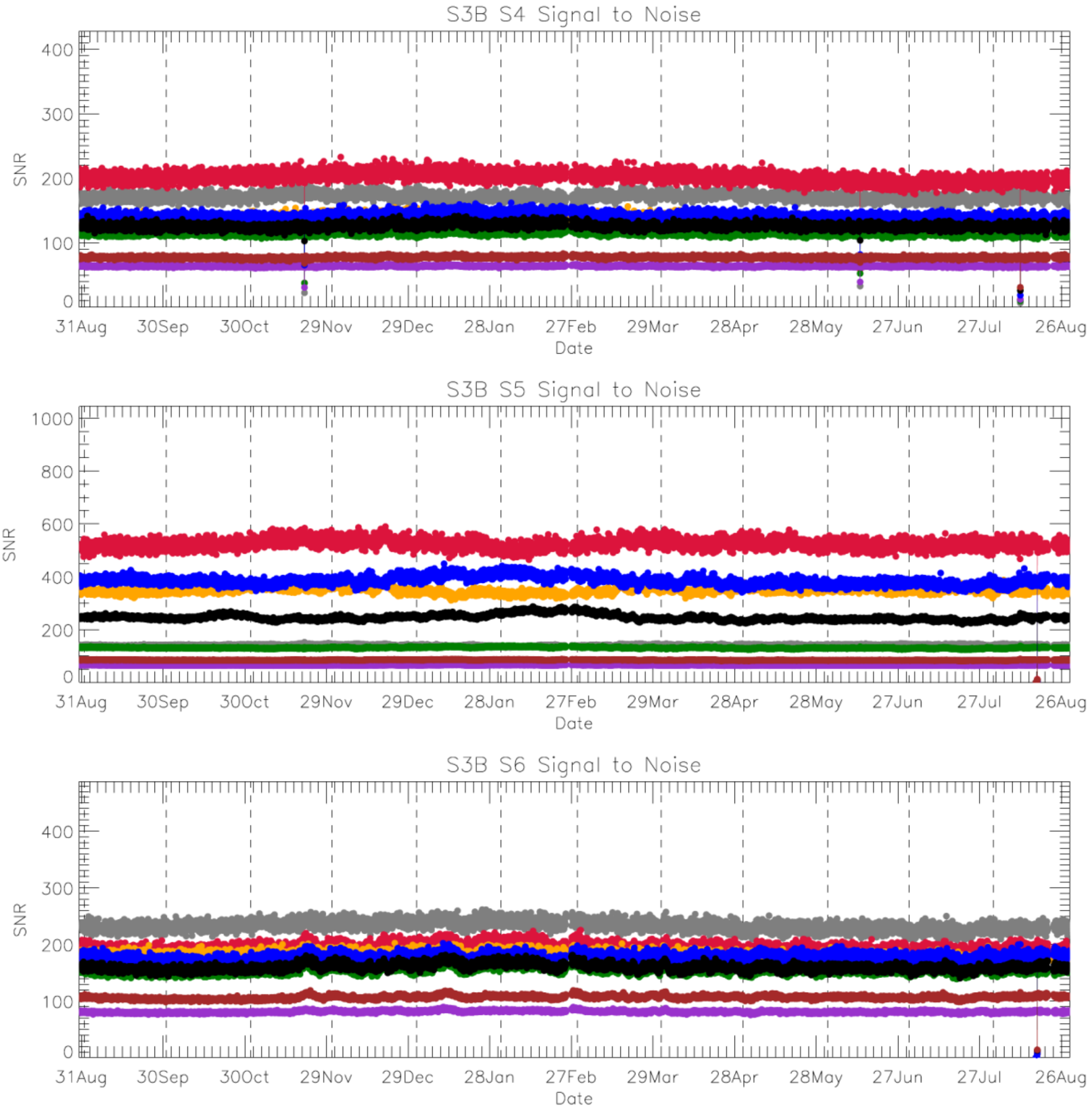

Figure 13. SWIR channel signal-to-noise of the measured VISCAL signal in each orbit for the last year of operations for SLSTR-B. Different colours indicate different detectors. The vertical dashed lines indicate the start of each month.

4.5.3 SLSTR-A TIR channel NEDT

The thermal channel NEDT values for SLSTR-A in August 2023 are consistent with previous operations and within the requirements. NEDT trends calculated from the hot and cold blackbody signals are shown in Figure 14. Monthly NEDT values, averaged over all detectors and both Earth views, are shown in Table 5.

TIR NEDT over the month

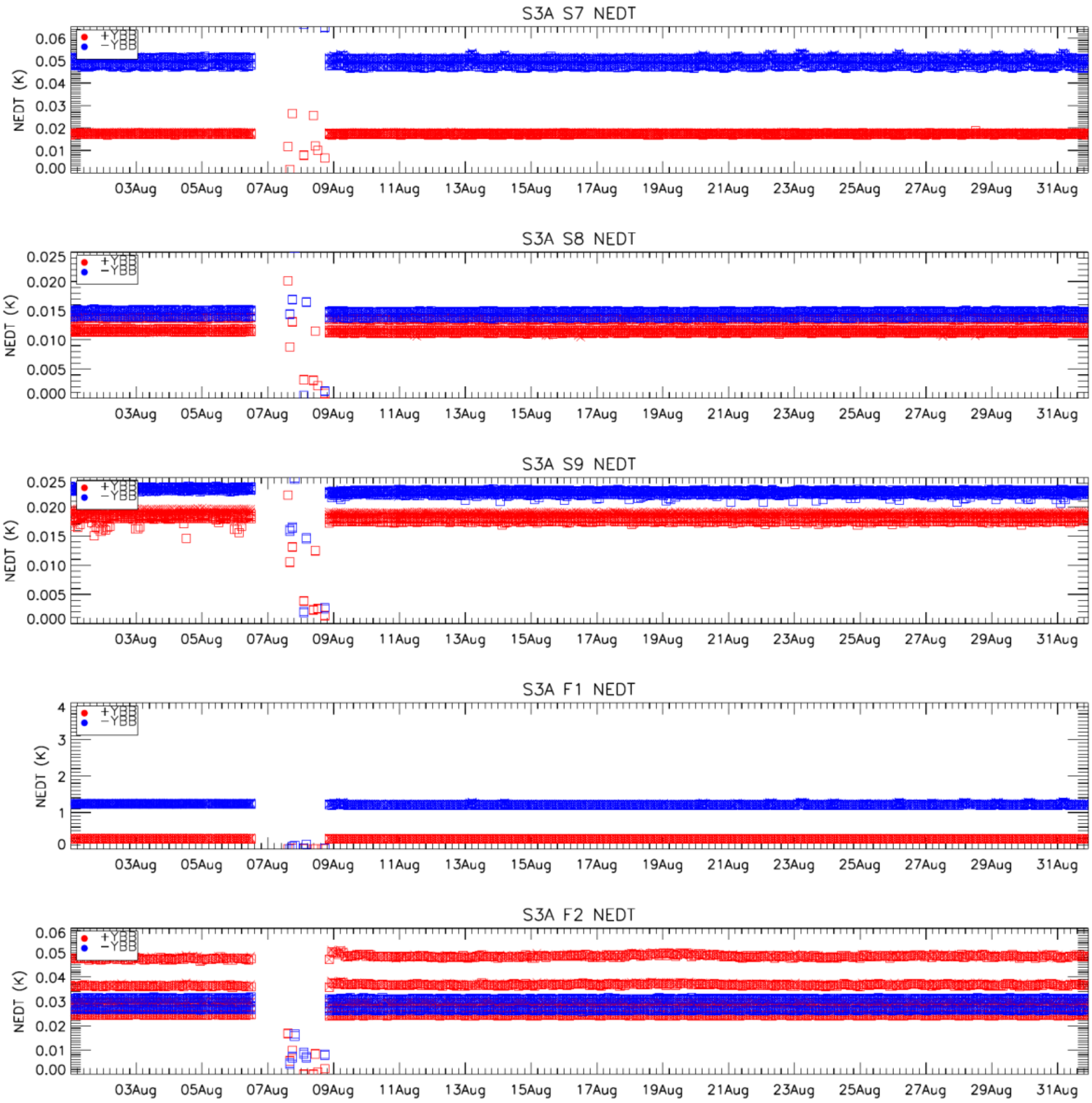

Figure 14: SLSTR-A NEDT trend for the thermal channels in August 2023. Blue points were calculated from the cold blackbody signal and red points from the hot blackbody. The square symbols show results calculated from the nadir view and crosses show results from the oblique view. Results are plotted for all detectors and integrators, which is why there are several different levels within the same colour points (particularly for S8 and F2).

Table 5: NEDT for SLSTR-A in the last 11 months averaged over all detectors for both Earth views towards the hot +YBB (top) and the cold -YBB (bottom).

SLSTR-A		**Oct 2022**	**Nov 2022**	**Dec 2022**	**Jan 2023**	**Feb 2023**	**Mar 2023**	**Apr 2023**	**May 2023**	**June 2023**	**July 2023**	**Aug 2023**
+YBB temp (K)		303.014	303.592	303.793	303.727	303.447	302.983	302.692	302.584	302.498	302.385	302.363
NEDT (mK)	**S7**	17.4	17.3	17.1	17.2	17.2	17.4	17.6	17.6	17.6	17.6	17.5
	S8	12.0	12.0	12.0	12.0	12.0	12.0	12.1	12.1	12.1	12.1	11.9
	S9	18.4	18.5	18.4	18.5	18.5	18.5	18.6	18.6	18.6	18.7	18.3
	F1	282	279	278	279	279	284	288	290	290	290	284
	F2	34.9	35.2	35.4	35.3	35.3	34.9	34.8	34.7	34.6	34.6	34.5

SLSTR-A		**Oct 2022**	**Nov 2022**	**Dec 2022**	**Jan 2023**	**Feb 2023**	**Mar 2023**	**Apr 2023**	**May 2023**	**June 2023**	**July 2023**	**Aug 2023**
-YBB temp (K)		265.867	266.569	266.812	266.695	266.319	265.801	265.594	265.630	265.589	265.224	265.201
NEDT (mK)	**S7**	49.6	48.5	47.6	48.0	48.5	49.4	50.1	50.4	50.2	49.8	49.9
	S8	14.6	14.6	14.6	14.6	14.6	14.7	14.7	14.7	14.7	14.7	14.6
	S9	22.7	22.7	22.6	22.7	22.7	22.8	22.9	23.0	23	23.1	22.6
	F1	1211	1176	1155	1169	1186	1218	1236	1245	1247	1243	1219
	F2	28.8	28.8	28.8	28.9	28.9	28.9	29.0	29.1	29.0	29.0	28.7

4.5.4 SLSTR-B TIR channel NEDT

The thermal channel NEDT values for SLSTR-B in August 2023, calculated from the hot and cold blackbody signals are shown in Figure 15 with monthly averages in Table 6. The thermal channel NEDT values for SLSTR-B in August 2023 are consistent with previous operations and within the requirements. Note that these averages are now calculated for each calendar month, whereas in data quality reports before January 2022 they were aligned to the satellite 27-day repeat cycles.

TIR NEDT over the month

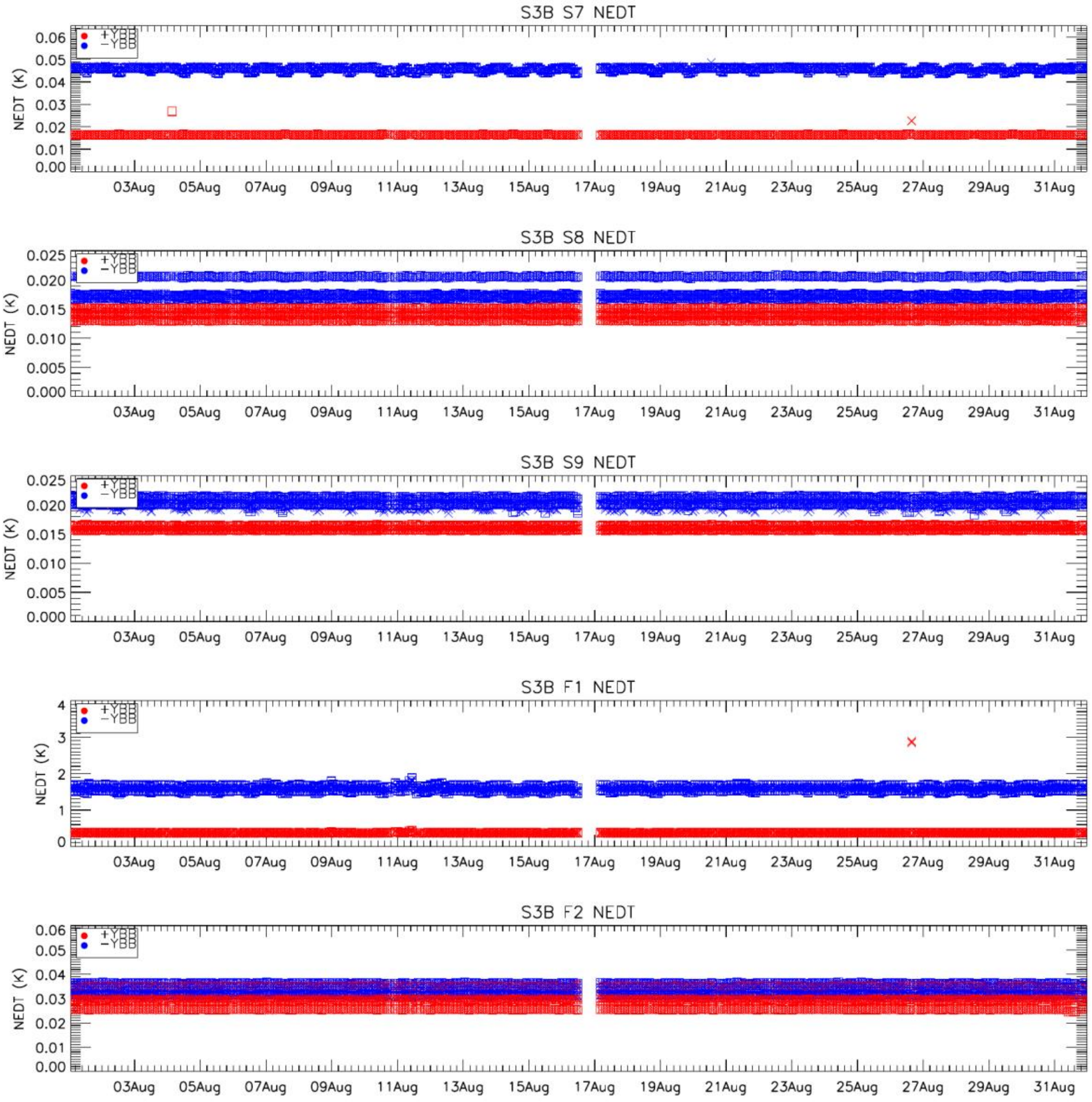

Figure 15: SLSTR-B NEDT trend for the thermal channels in August 2023. Blue points were calculated from the cold blackbody signal and red points from the hot blackbody. The square symbols show results calculated from the nadir view and crosses show results from the oblique view. Results are plotted for all detectors and integrators, which is why there are several different levels within the same colour points (particularly for S8 and F2).

Table 6: NEDT for SLSTR-B in the last 11 months averaged over all detectors for both Earth views towards the hot +YBB (top) and the cold -YBB (bottom).

SLSTR-B		Oct 2022	Nov 2022	Dec 2022	Jan 2023	Feb 2023	Mar 2023	Apr 2023	May 2023	Jun 2023	Jul 2023	Aug 2023
+YBB temp (K)		303.138	303.596	303.894	303.850	303.489	303.074	302.754	302.668	302.572	302.452	302.445
NEDT (mK)	**S7**	16.8	16.2	16.1	16.0	16.1	16.2	16.5	16.5	16.5	16.5	16.5
	S8	14.1	14.0	14.3	13.9	14.0	14.0	14.0	14.0	14.0	14.1	14.1
	S9	16.0	15.9	16.5	15.9	16.0	15.8	15.8	15.9	15.9	16.0	16.0
	F1	375	350	345	349	369	367	368	367	369	374	378
	F2	30.4	30.4	30.6	30.5	30.4	30.2	30.3	30.3	30.2	30.1	30.1

SLSTR-B		Oct 2022	Nov 2022	Dec 2022	Jan 2023	Feb 2023	Mar 2023	Apr 2023	May 2023	Jun 2023	Jul 2023	Aug 2023
-YBB temp (K)		265.525	266.220	266.554	266.431	265.924	265.360	265.131	265.196	265.146	264.944	264.842
NEDT (mK)	**S7**	43.3	43.2	42.9	42.8	43.7	44.6	44.5	44.3	44.8	45.5	45.8
	S8	17.8	17.9	17.9	18.0	18.0	17.8	17.8	17.9	17.9	18.0	18.0
	S9	20.2	20.4	20.4	20.4	20.5	20.2	20.3	20.3	20.4	20.4	20.5
	F1	1441	1435	1427	1430	1564	1550	1525	1502	1529	1571	1591
	F2	33.1	33.1	33.1	33.2	33.3	33.1	33.1	33.2	33.3	33.4	33.4

4.6 Calibration factors

4.6.1 VIS and SWIR radiometric response

The radiometric gain derived from the VISCAL signals over the past year are shown in this section. It should be noted that the data from the VISCAL unit and blackbodies calibrates the signal and counteracts the degradation of the optics and other variations in signal observed in the plots.

There are several features that appear in this parameter that can be explained as:

- The visible channels show oscillations in their radiometric response due to the build-up of ice on the optical path within the focal plane assembly (FPA). Similar oscillations were observed for the corresponding channels on ATSR-2 and AATSR. As described in Section 4.2, periodic decontamination of the infrared FPA is necessary to remove the water ice contamination.
- The radiometric responses of the SWIR channels appear to be more stable and not affected by the build-up of water ice contamination, although there is a seasonal cycle of the response that could be caused by variations in the solar zenith angle on the diffuser or partial vignetting of the Sun's disc by the VISCAL baffle.
- Note that the period of the oscillations depends on the rate of build up of the ice layer, which is faster for SLSTR-B because it has had less time to decontaminate.

4.6.2 SLSTR-A

Figure 16 and Figure 17 show the variation of the radiometric gain derived from the VISCAL signals for SLSTR-A over the past year. The data from the last month appears normal and follows the expected trend. The following features in this annual trend plot should be noted:

- August 2023: an anomaly occurred on the instrument on 6th August, which was recovered with a power cycle and decontamination/cooldown. This causes a discontinuity in the gain due to the reduction in water ice after the decontamination.

VIS VISCAL signal variation over the past year

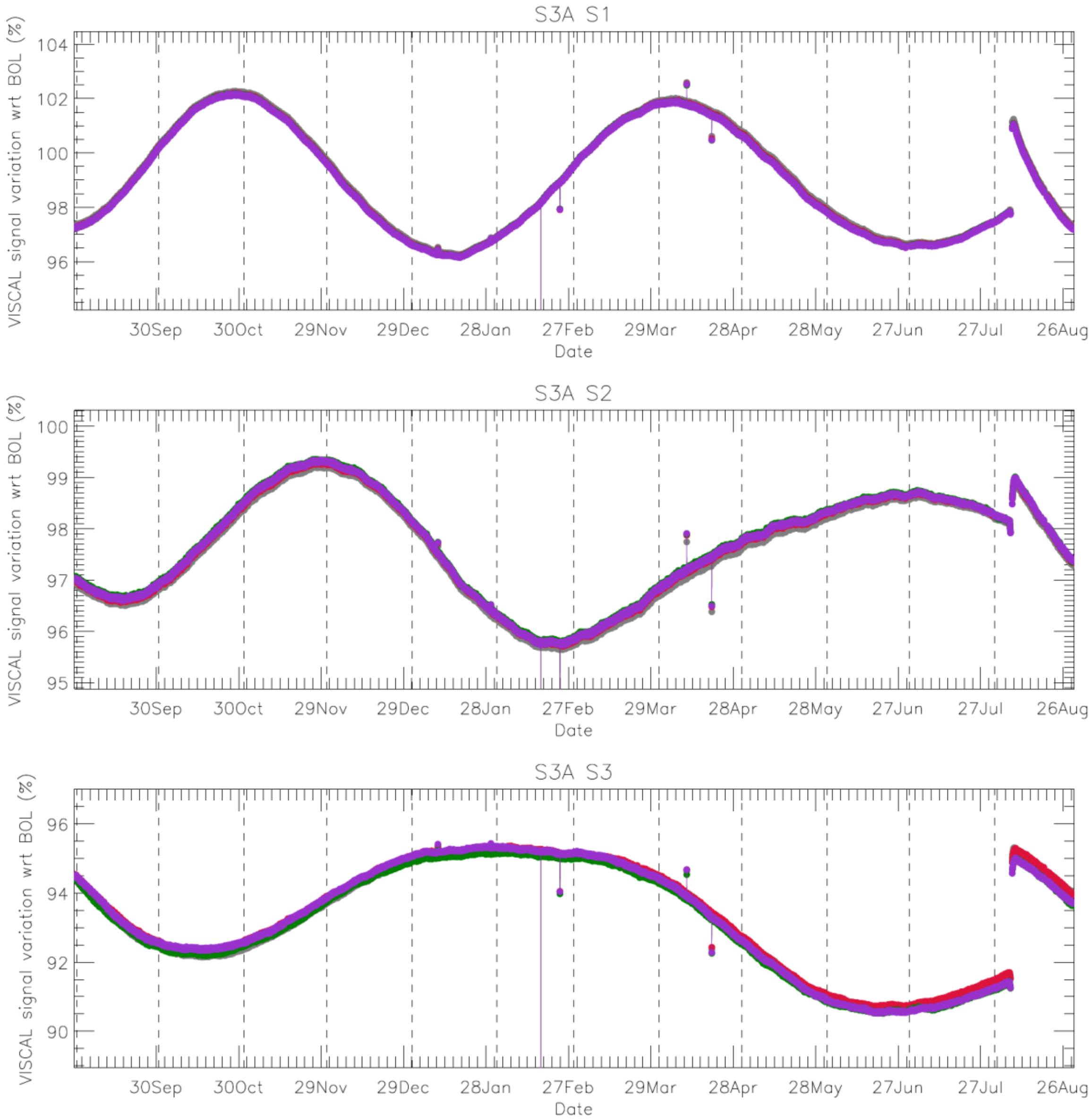

Figure 16: Variation of the radiometric gain derived from the VISCAL signals for SLSTR-A VIS channels for the last year of operations (nadir view). Different colours represent different detectors. The vertical dashed lines indicate the start of each month.

SWIR VISCAL signal variation over the past year

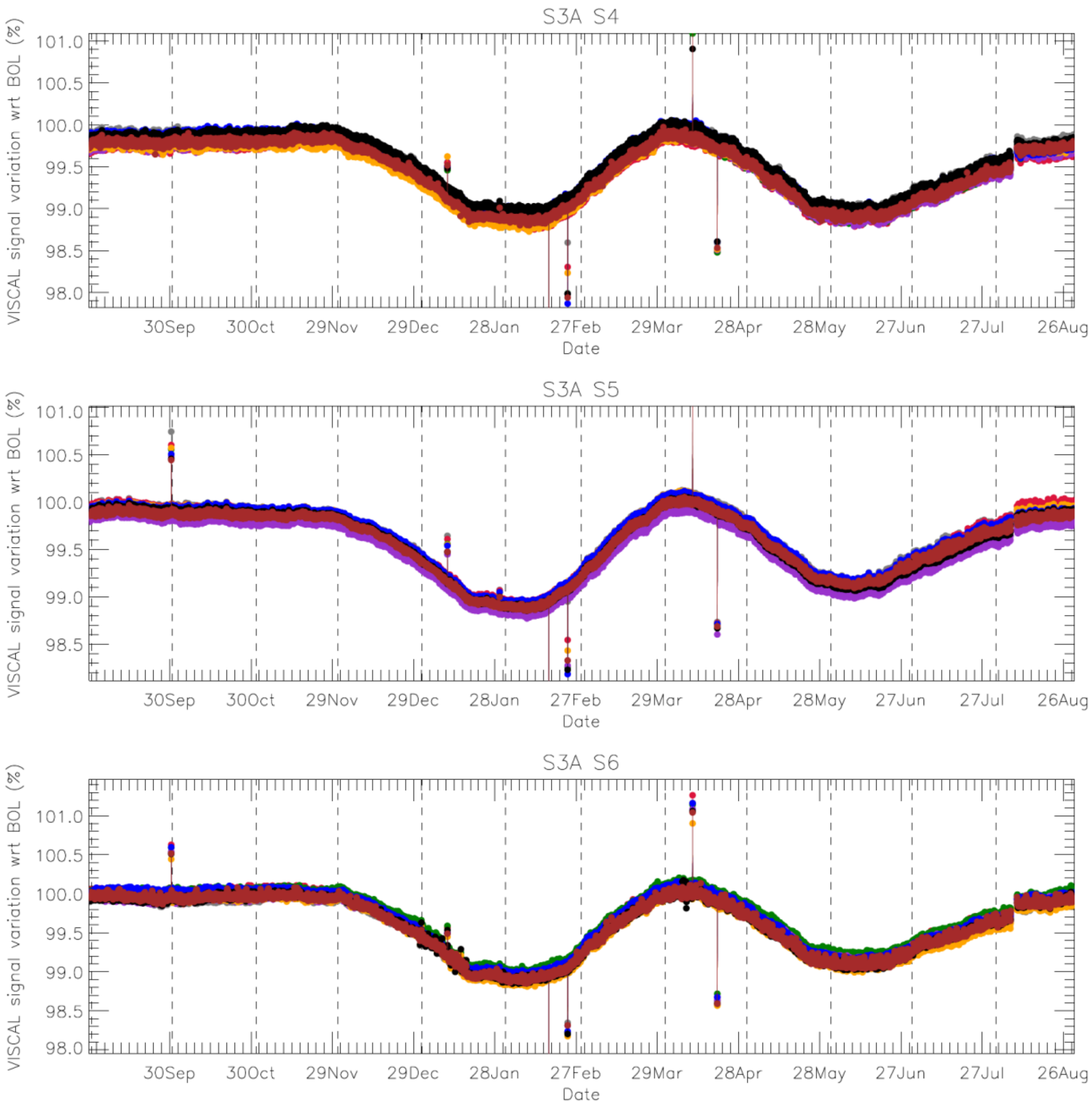

Figure 17: Variation of the radiometric gain derived from the VISCAL signals for SLSTR-A SWIR channels for the last year of operations (nadir view). Different colours represent different detectors. The vertical dashed lines indicate the start of each month.

4.6.3 SLSTR-B

Figure 18 and Figure 19 show the variation of the radiometric gain derived from the VISCAL signals for SLSTR-B over the past year. The data from the last month appears normal and follows the expected trend. There are several features in this annual trend plot to note.

- There is noisy behaviour and numerous drops in signal in the radiometric gain, especially in channels S1 and S2. This gives 2-3% errors in the radiometric calibration of these channels. A number of candidate root causes have been identified, with the most likely due to motional chopping of the VIS detectors by an internal aperture in the VIS optical bench. Because the effect appears to be random it is most likely affecting all the data for S1 and S2.

VIS VISCAL signal variation over the past year

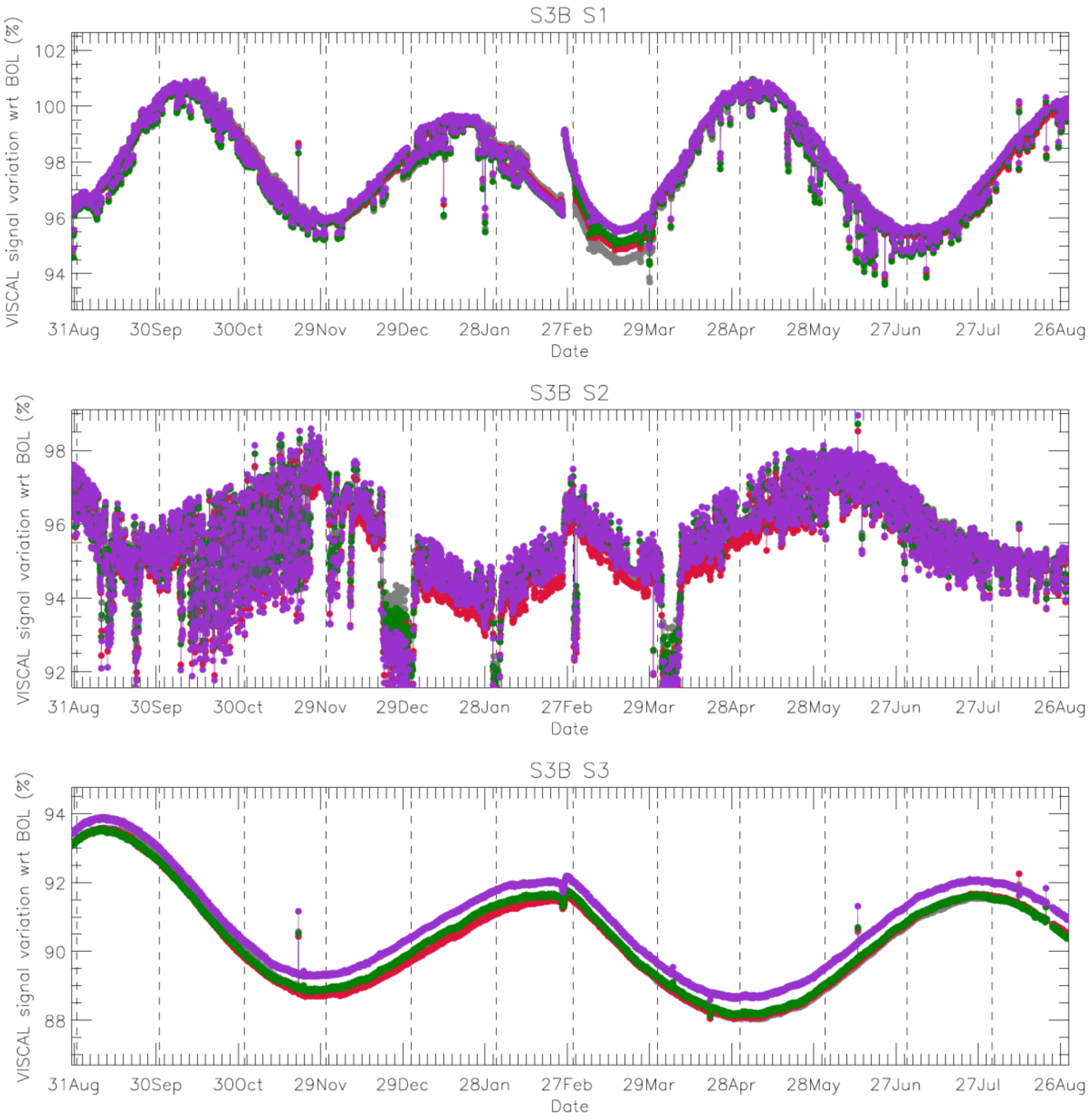

Figure 18: Variation of the radiometric gain derived from the VISCAL signals for SLSTR-B VIS channels for the past year (nadir view). Different colours represent different detectors. The vertical dashed lines indicate the start of each month.

SWIR VISCAL signal variation over the past year

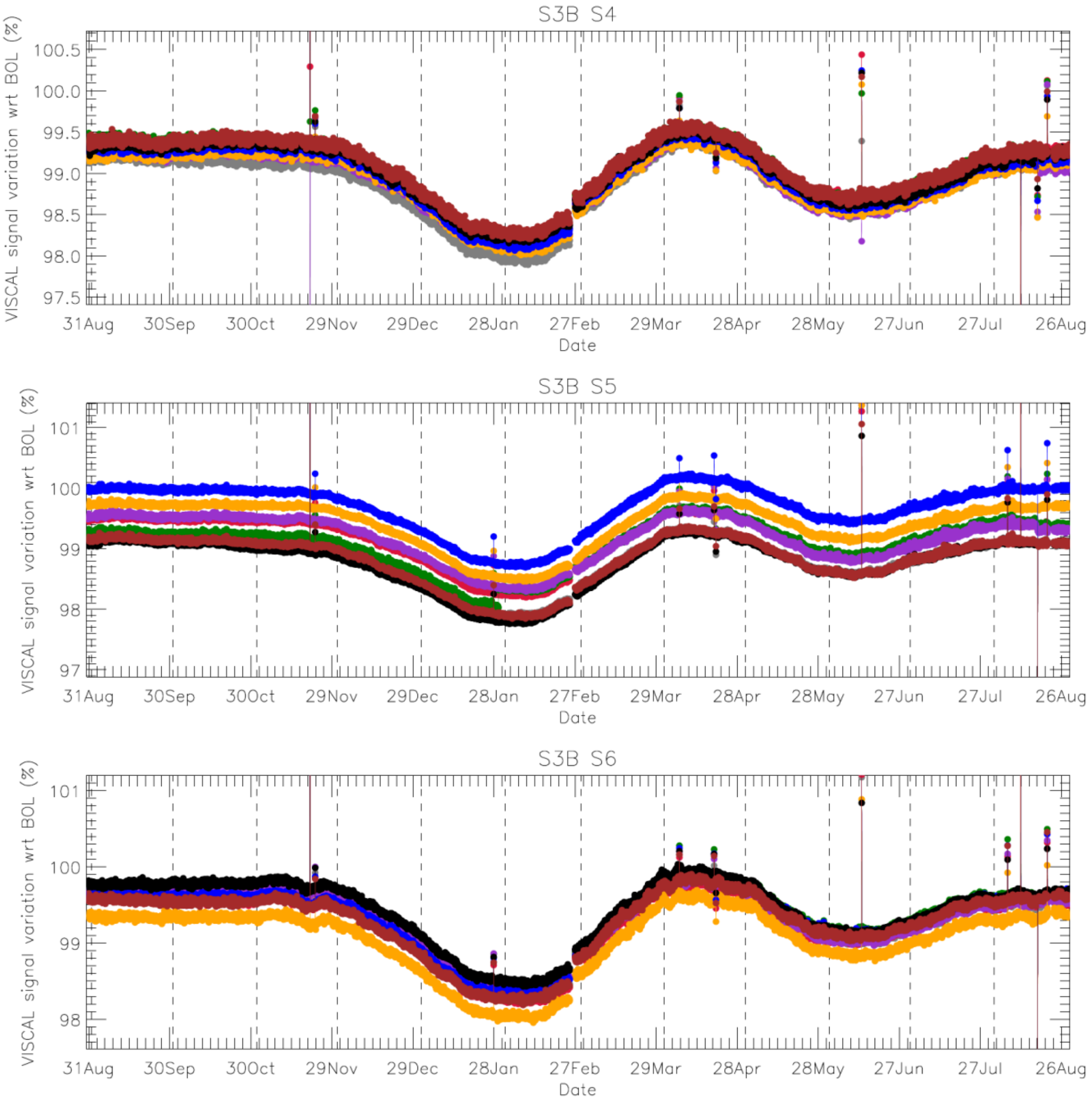

Figure 19: Variation of the radiometric gain derived from the VISCAL signals for SLSTR-B SWIR channels for the past year (nadir view). Different colours represent different detectors. The vertical dashed lines indicate the start of each month.

5 Level-1 product validation

Level-1 product quality is assessed in terms of radiometric and geometric accuracy

The Level-1 image quality is assessed when data are available at the MPC. For example, by combining all granules over one day into a single combined image. The S3A and S3B satellites are configured to be 140 degrees out of phase in order to observe complimentary portions of the earth. Figure 20 shows an example combined SLSTR-A/SLSTR-B image for the visible channels on 2nd of September 2023 (daytime only).

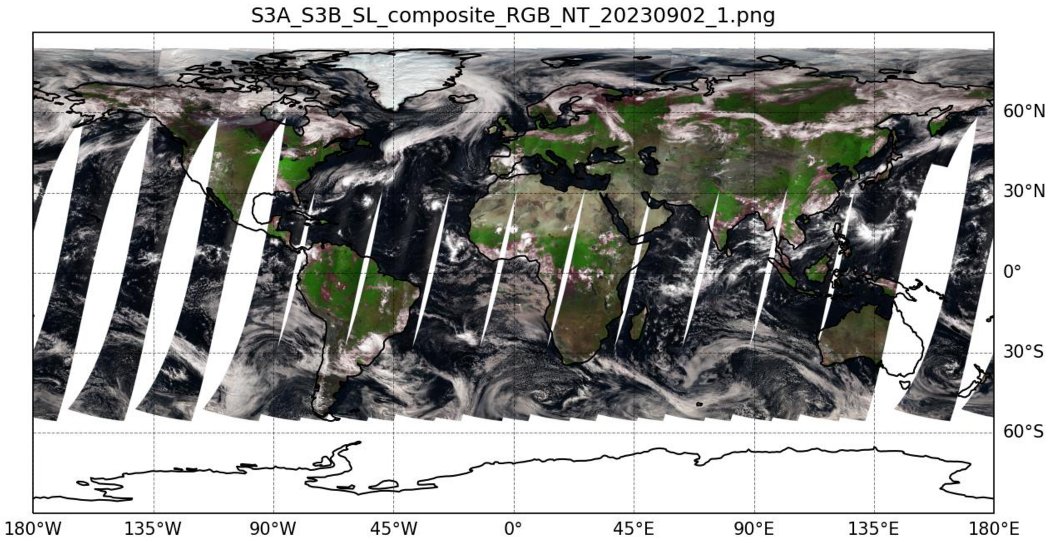

Figure 20: Daytime combined SLSTR-A and SLSTR-B Level-1 image for visible channels on 2nd of September 2023.

5.1 Level-1 TIR Radiometric Validation

S3_MR_1000 Relative radiometric accuracy: Sentinel-3 infrared channels shall have a relative radiometric accuracy of <0.08K (threshold) with a goal of 0.05 K over a range of 210-350 K expressed as NEDT traceable to international reference standards.

The absolute radiometric calibration of the IR channels is being validated by EUMETSAT using comparisons against IASI-A and B (Tomazic et al 2018). These results confirmed very good performance with almost no bias (< 0.1 K) for channels S8 and S9 in the nadir view over the temperature range 220 – 280 K.

5.2 Level- 1 VIS SWIR Radiometric Validation

A3_MR_1010 Absolution radiometric accuracy: Sentinel-3 VIS reflectance at TO shall have an absolute radiometric accuracy goal of < 2% with reference to the sun for the 400-900 nm wavebands and <5% with reference to the sun for wavebands >900 nm traceable to international reference standards.

Validation of the VIS/SWIR radiometric measurements is performed by various methods to establish the magnitude of any calibration offset. Some activities are routinely performed each month and reported here, and some are less regular and reported in the annual data quality reports.

The results of these different methods have been collated and have been found to agree that there is a calibration offset present in the VIS/SWIR radiances. It is recommended therefore that users apply an offset in-line with the values presented in Table 7. These offsets are stable and apply to the entire mission. Note that uncertainty estimates are at k=1.

Nadir View	**S1**	**S2**	**S3**	**S5**	**S6**
Correction	0.97	0.98	0.98	1.11	1.13
Uncertainty	0.03	0.02	0.02	0.02	0.02
Oblique View	**S1**	**S2**	**S3**	**S5**	**S6**
Correction	0.94	0.95	0.95	1.04	1.07
Uncertainty	0.05	0.03	0.03	0.03	0.05

Table 7. The recommended corrections that should be applied to SLSTR-A and SLSTR-B VIS, SWIR channels.

5.2.1 S3ETRAC latest mission trend SLSTR-A and SLSTR-B

The radiometric calibration of the visible and SWIR channels is routinely monitored using the S3ETRAC service. SLSTR data is compared to three different satellite instruments over these sites, with average ratios in each case are given in the figures.

- Figure 21 shows the results of the inter-comparison analysis of SLSTR-A with OLCI-A and SLSTR-B with OLCI-B over desert sites.
- Figure 22 shows the results of an inter-comparison analysis of SLSTR-A and SLSTR-B with AATSR.
- Figure 23 shows the results of the inter-comparison analysis with MODIS.

The results presented in the current issue refer to the period of December 2022.

A year-by-year breakdown of the drift in % since the start of the mission for SLSTR-A is provided in Table 8. Uncertainty in the drift rate is estimated at 1%.

Table 8. A year-by-year breakdown of the drift in % since the start of the mission for SLSTR-A Note the trends for S6 are based on comparisons with MODIS-Aqua which are limited to June-July where the geometry matches.

	S1		S2		S3		S5a		S5b		S6a		S6b	
Year	**Na**	**Ob**	**Na**	**Ob**	**Na**	**Ob**	**Na**	**Ob**	**Na**	**Ob**	**Na**	**Ob**	**Na**	**Ob**
2017	0.3	0.0	0.2	0.3	0.5	0.5	0.1	0.0	0.2	0.1	0.1	-	0.0	-
2018	0.7	1.0	0.2	0.3	0.8	0.9	0.0	-0.1	0.0	-0.1	-0.6	-	-0.7	-
2019	0.9	0.5	0.4	0.4	1.1	1.2	0.0	0.0	0.0	0.0	-0.2	-	-0.3	-
2020	1.1	0.7	0.6	0.5	1.4	1.6	0.0	-0.1	0.0	-0.1	-0.2	-	-0.3	-
2021	1.4	0.9	0.6	0.6	1.6	1.8	0.0	0.0	0.0	0.0	-0.2	-	-0.3	-
2022	2.2	1.3	1.1	0.7	2.2	2.3	0.2	0.0	0.2	0.0	0.7	-	0.6	-

A year-by-year breakdown of the drift in % since the start of the mission for SLSTR-B is provided in Table 9. Uncertainty in the drift rate is estimated at 1%.

Table 9. A year-by-year breakdown of the drift in % since the start of the mission for SLSTR-B. Note the trends for S6 are based on comparisons with MODIS-Aqua which are limited to June-July where the geometry matches. Furthermore, the drift for S6 is relative to 2019 comparisons. For SLSTR-B the reference measurements were obtained before an update to the flight calibration coefficients that was performed after the S3B-IOCR. A correction factor of 2.4% has been applied to the drift rates to account for the update.

	S1		S2		S3		S5a		S5b		S6a		S6b	
Year	**Na**	**Ob**	**Na**	**Ob**	**Na**	**Ob**	**Na**	**Ob**	**Na**	**Ob**	**Na**	**Ob**	**Na**	**Ob**
2019	0.7	-1.2	0.5	-0.3	0.3	0.0	0.2	-0.1	0.3	-1.1	-	-	-	-
2020	0.9	-0.8	0.5	-0.2	0.5	0.4	0.3	-0.3	0.3	-1.3	-0.2	-	-0.2	-
2021	1.3	-0.4	0.7	0.2	0.8	0.7	0.3	-0.3	0.2	-1.3	0.0	-	-0.1	-
2022	2.1	-0.5	1.2	-0.1	1.5	1.2	0.7	-0.2	0.6	-1.2	1.0	-	0.9	-

The S3ETRAC service extracts OLCI and SLSTR Level-1 data and computes associated statistics over 49 sites corresponding to different surface types (desert, snow, ocean maximising Rayleigh signal, and ocean maximising sun-glint scattering). These S3ETRAC products are used for the assessment and monitoring of the VIS and SWIR radiometry by the ESL.

Details of the S3ETRAC/SLSTR statistics are provided on the S3ETRAC website, including:

- Number of SLSTR products processed by the S3ETRAC service
- Statistics per type of target (DESERT, SNOW, RAYLEIGH, SUNGLINT)
- Statistics per site
- Statistics on the number of records

Latest mission trend of SLSTR vs OLCI

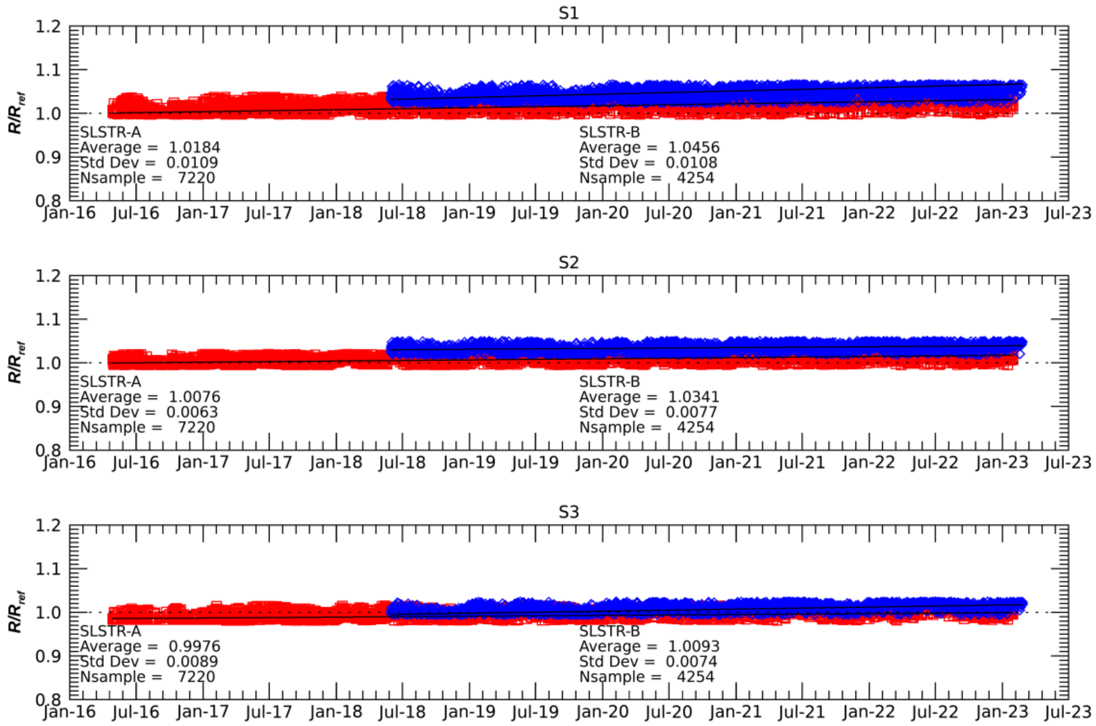

Figure 21: Ratio of SLSTR-A and OLCI-A radiances (red) and SLSTR-B and OLCI-B radiances (blue) for the visible channels in Nadir view using combined results for all desert sites.

Latest Mission trend of SLSTR vs AATSR

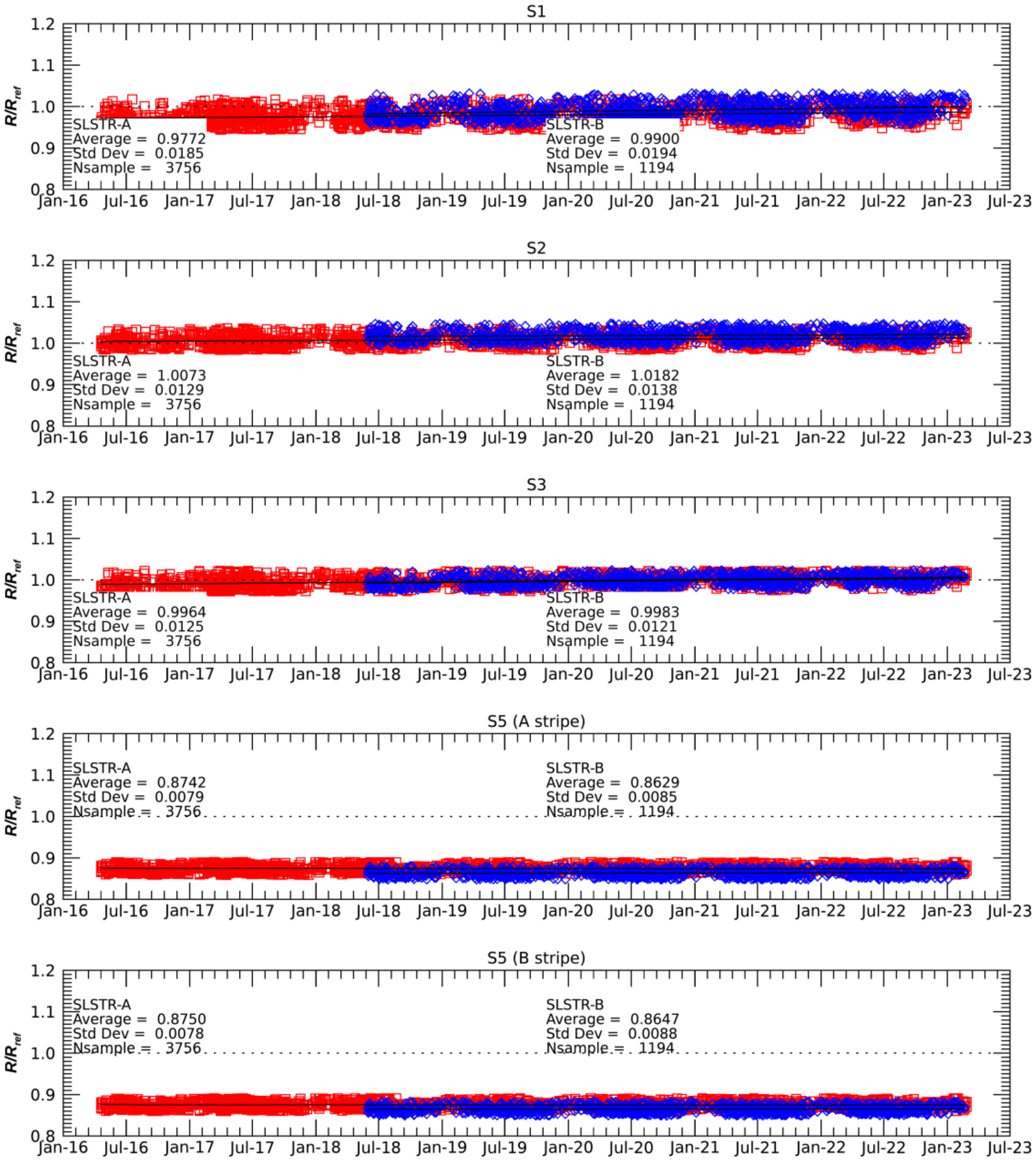

Figure 22: Ratio of SLSTR-A (red) and SLSTR-B (blue) with AATSR radiances in Nadir view using combined results for all desert sites.

Latest Mission trend of SLSTR vs MODIS

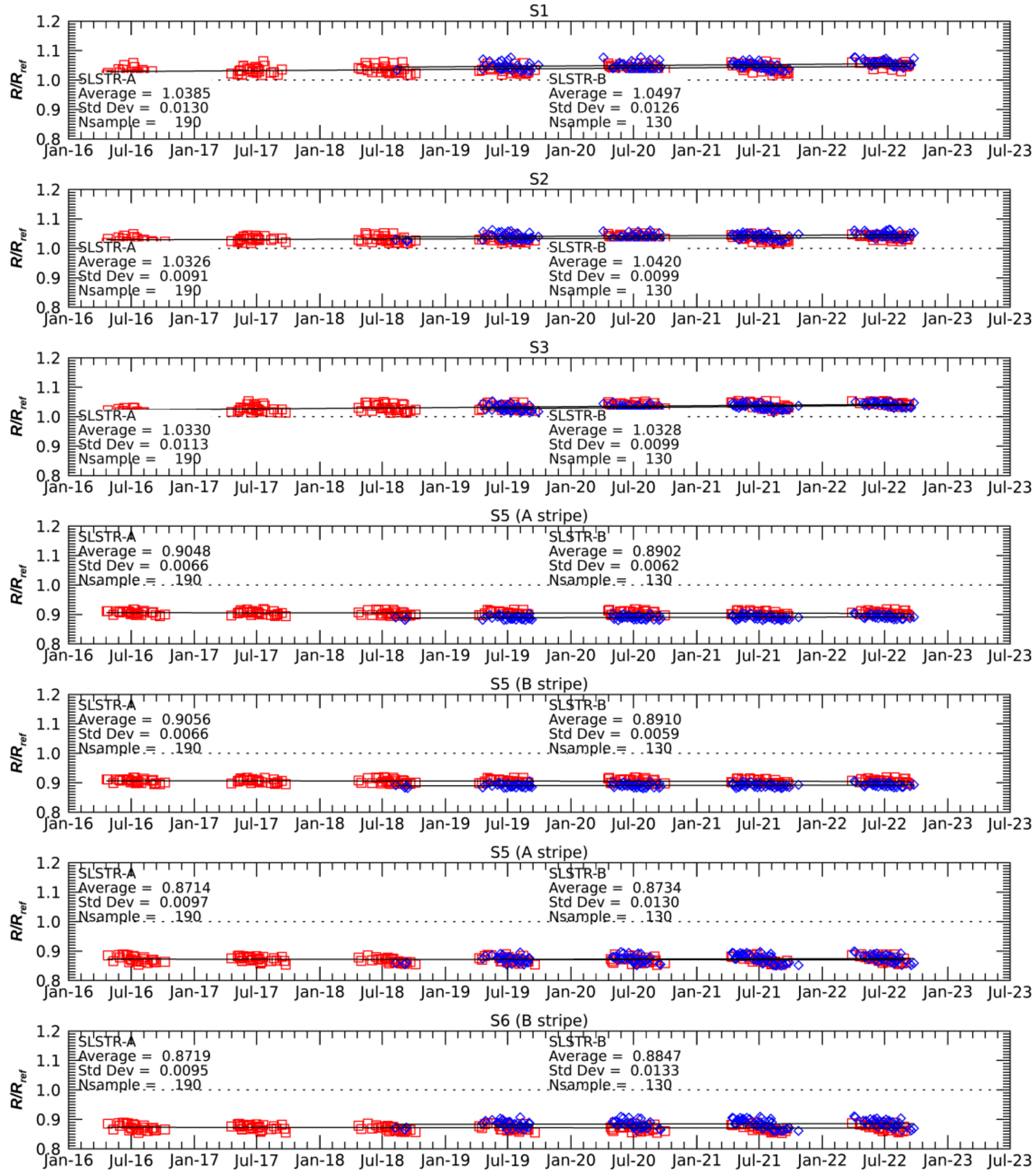

Figure 23: Ratio of SLSTR-A (red) and SLSTR-B (blue) with MODIS radiances in Nadir view using combined results for all desert sites.

5.2.2 Radiometric validation with DIMITRI

Verification and Validation over PICS

1. The ingestion of the available L1-RBT-NT products from SLSTR-A and SLSTR-B over the 6 desert CalVal-sites (Algeria3 & 5, Libya 1 & 4 and Mauritania 1 & 2) has been performed until the **31st August 2023**.
2. The results are consistent over all the six used PICS sites (Figure 24 and Figure 25). Both sensors show a good stability over the analysed period over VNIR bands for both NADIR & OBLIQUE views, with slight positive trend.
3. The temporal average over the period **1st January 2023- 31st August 2023** of the elementary ratios (observed reflectance to the simulated one) for **SLSTR-A** and **SLSTR-B** show gain values between 4-6% (NADIR) and 7-9% (OBLIQUE) over the VNIR bands S1-S3 (Figure 26).

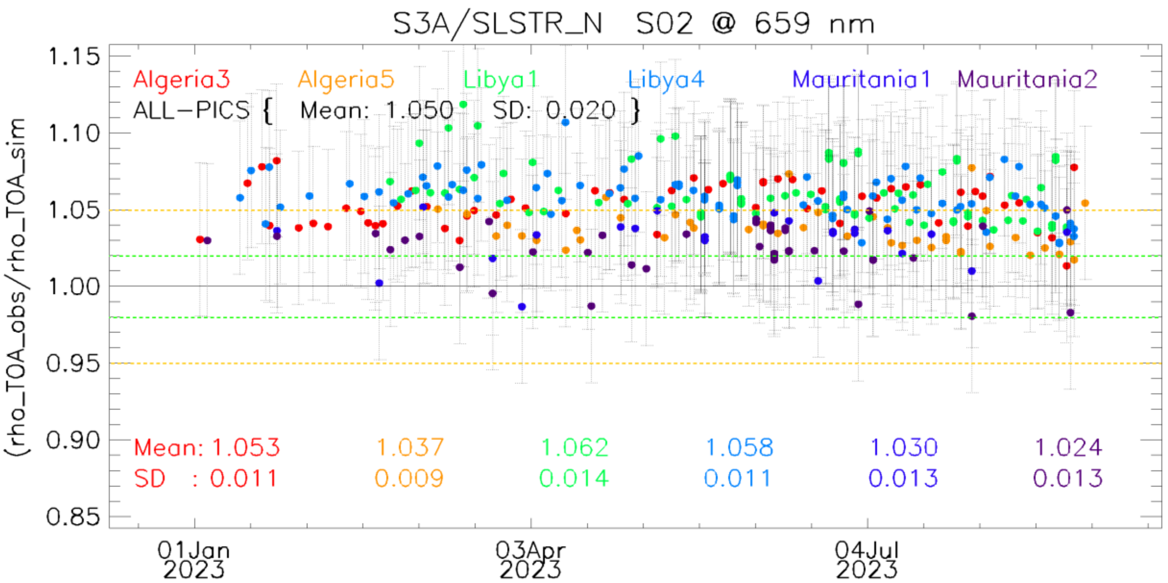
S3A/SLSTR_N S02 @ 659 nm
Algeria3
Algeria5
Libya1
Libya4
Mauritania1
Mauritania2
ALL−PICS { Mean: 1.050 SD: 0.020 }
Mean: 1.053
SD : 0.011
1.037
0.009
1.062
0.014
1.058
0.011
1.030
0.013
1.024
0.013
(rho_TOA_obs/rho_TOA_sim
1.15
1.10
1.05
1.00
0.95
0.90
0.85
01Jan 2023
03Apr 2023
04Jul 2023

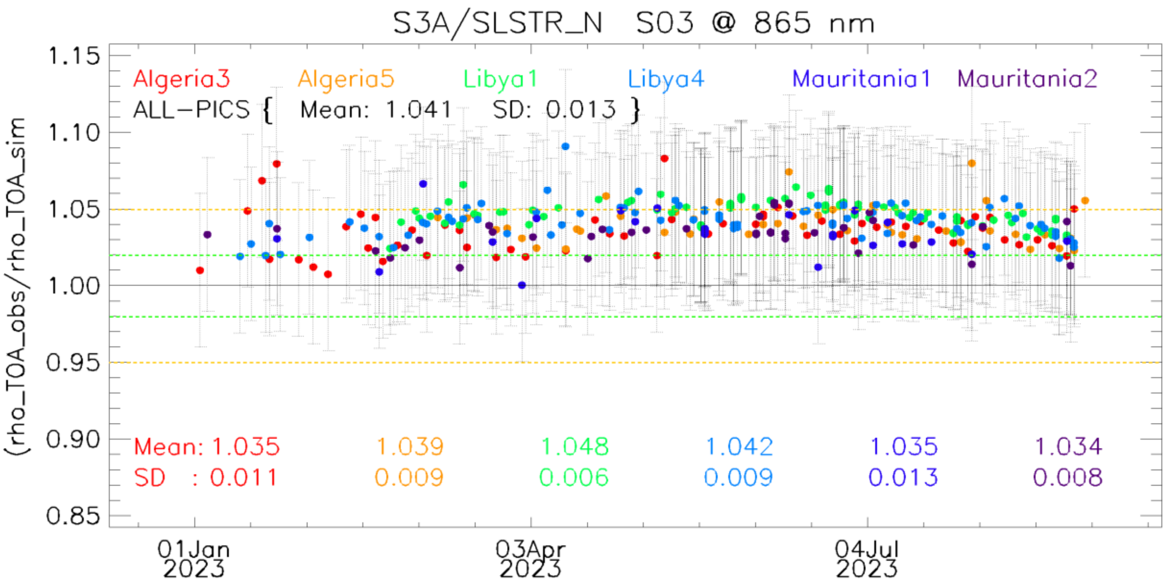
S3A/SLSTR_N S03 @ 865 nm
Algeria3
Algeria5
Libya1
Libya4
Mauritania1
Mauritania2
ALL−PICS { Mean: 1.041 SD: 0.013 }
Mean: 1.035
SD : 0.011
1.039
0.009
1.048
0.006
1.042
0.009
1.035
0.013
1.034
0.008
(rho_TOA_obs/rho_TOA_sim
1.15
1.10
1.05
1.00
0.95
0.90
0.85
01Jan 2023
03Apr 2023
04Jul 2023

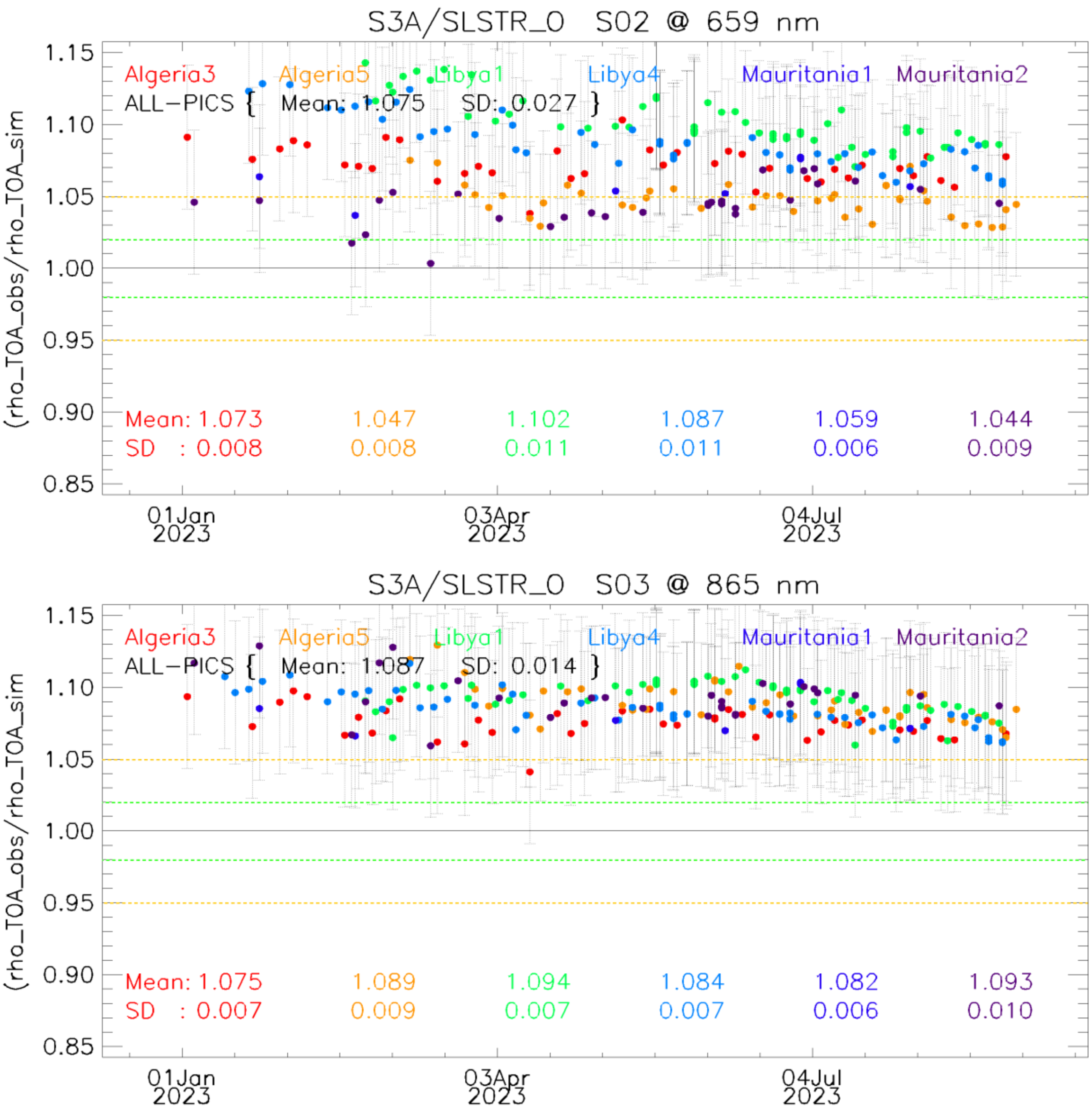

Figure 24: Time-series of the elementary ratios (observed/simulated) signal from SLSTR-A for (top to bottom) bands S02 and S03 (Nadir & Oblique views) respectively over January 2023- August 2023 from the six PICS Cal/Val sites. Dashed-green and orange lines indicate the 2% and 5% respectively. Error bars indicate the desert methodology uncertainty.

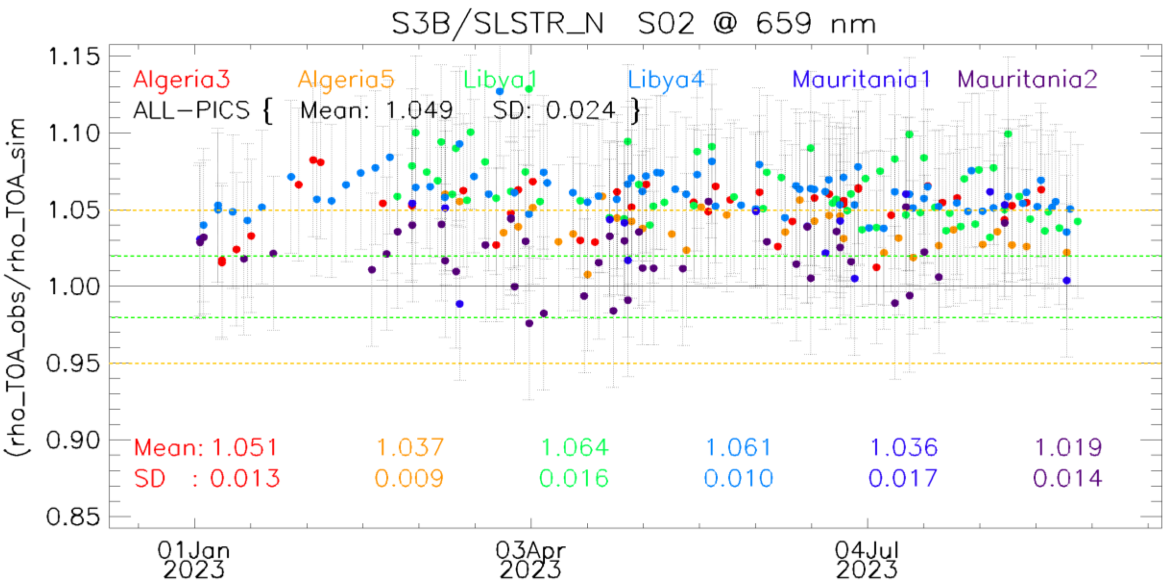
S3B/SLSTR_N S02 @ 659 nm
Algeria3
Algeria5
Libya1
Libya4
Mauritania1
Mauritania2
ALL−PICS { Mean: 1.049 SD: 0.024 }
Mean: 1.051
SD : 0.013
1.037
0.009
1.064
0.016
1.061
0.010
1.036
0.017
1.019
0.014
(rho_TOA_obs/rho_TOA_sim
1.15
1.10
1.05
1.00
0.95
0.90
0.85
01Jan 2023
03Apr 2023
04Jul 2023

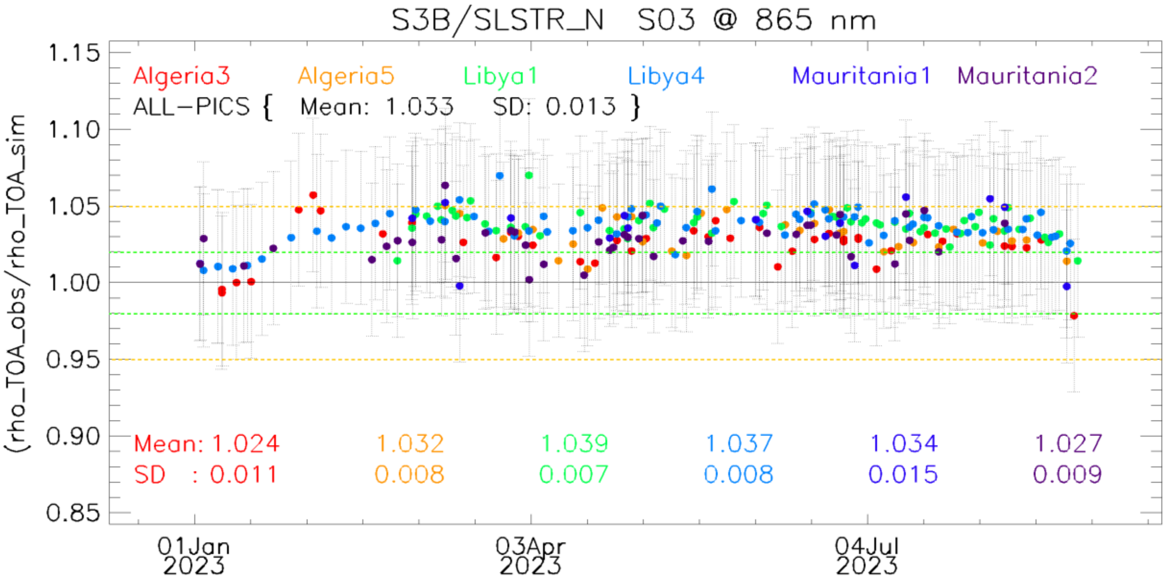
S3B/SLSTR_N S03 @ 865 nm
Algeria3
Algeria5
Libya1
Libya4
Mauritania1
Mauritania2
ALL−PICS { Mean: 1.033 SD: 0.013 }
Mean: 1.024
SD : 0.011
1.032
0.008
1.039
0.007
1.037
0.008
1.034
0.015
1.027
0.009
(rho_TOA_obs/rho_TOA_sim
1.15
1.10
1.05
1.00
0.95
0.90
0.85
01Jan 2023
03Apr 2023
04Jul 2023

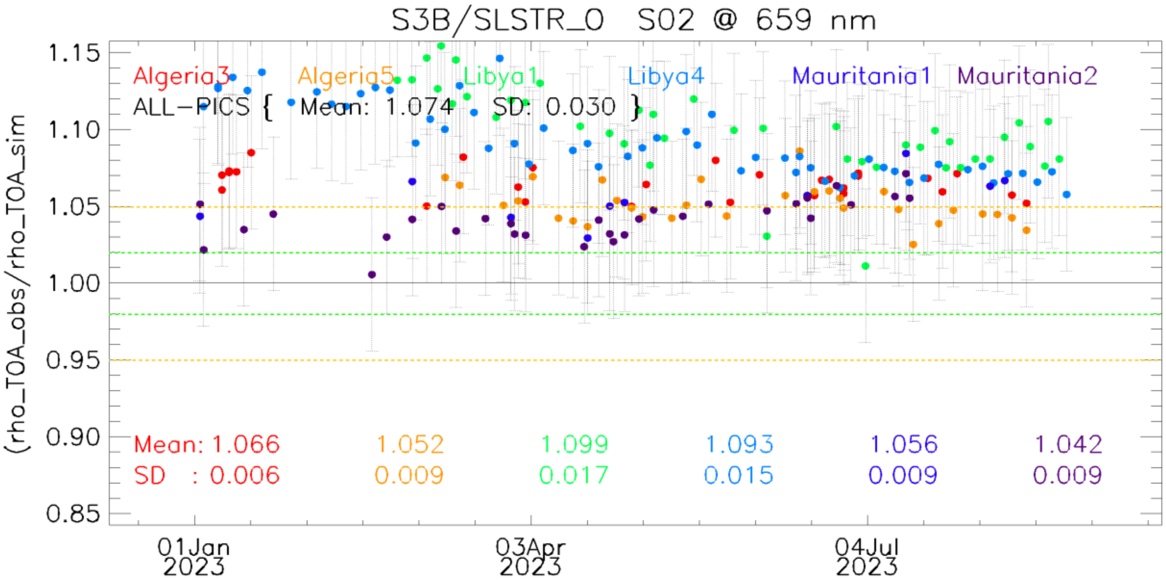

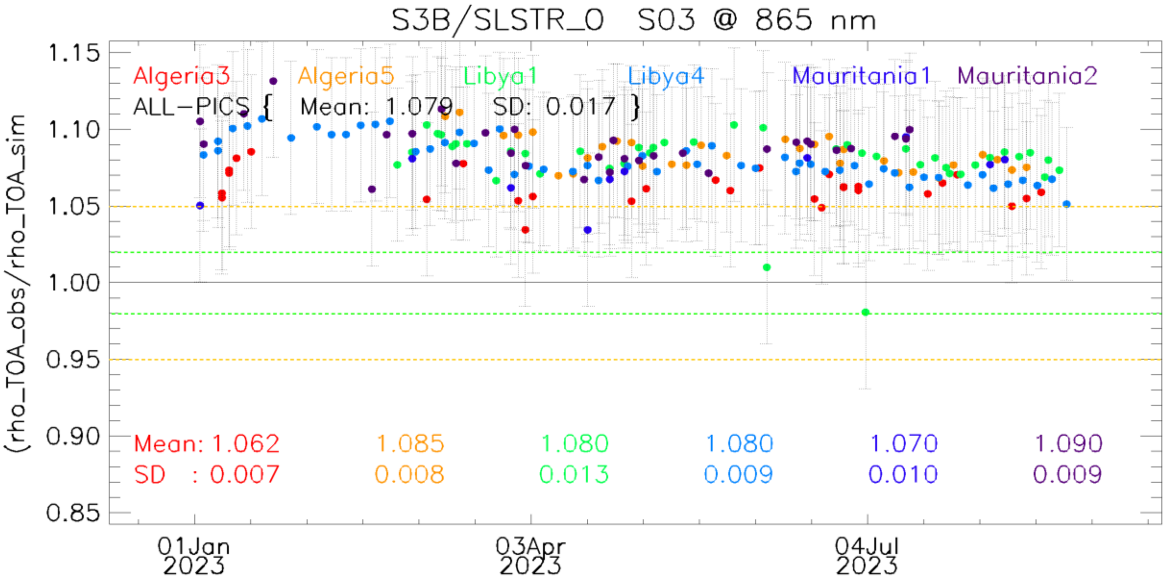

Figure 25:Time-series of the elementary ratios (observed/simulated) signal from SLSTR-B for (top to bottom) bands S02 and S03 (Nadir & Oblique views) respectively over January 2023- August 2023 from the six PICS Cal/Val sites. Dashed-green and orange lines indicate the 2% and 5% respectively. Error bars indicate the desert methodology uncertainty.

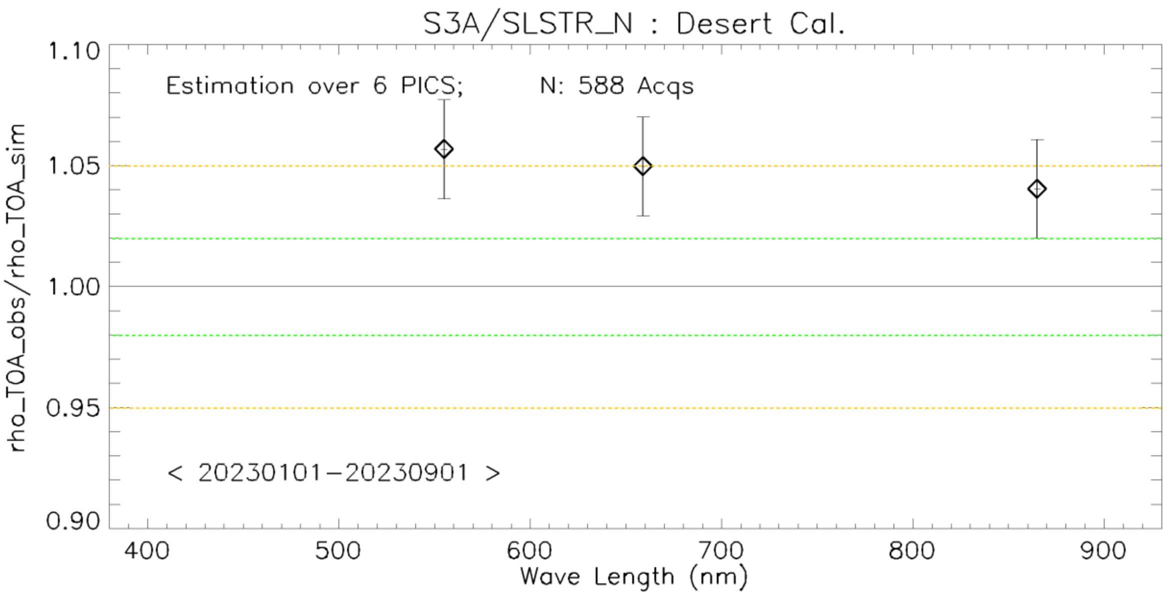
S3A/SLSTR_N : Desert Cal.
Estimation over 6 PICS; N: 588 Acqs
< 20230101–20230901 >
rho_TOA_obs/rho_TOA_sim
1.10
1.05
1.00
0.95
0.90
400
500
600
700
800
900
Wave Length (nm)

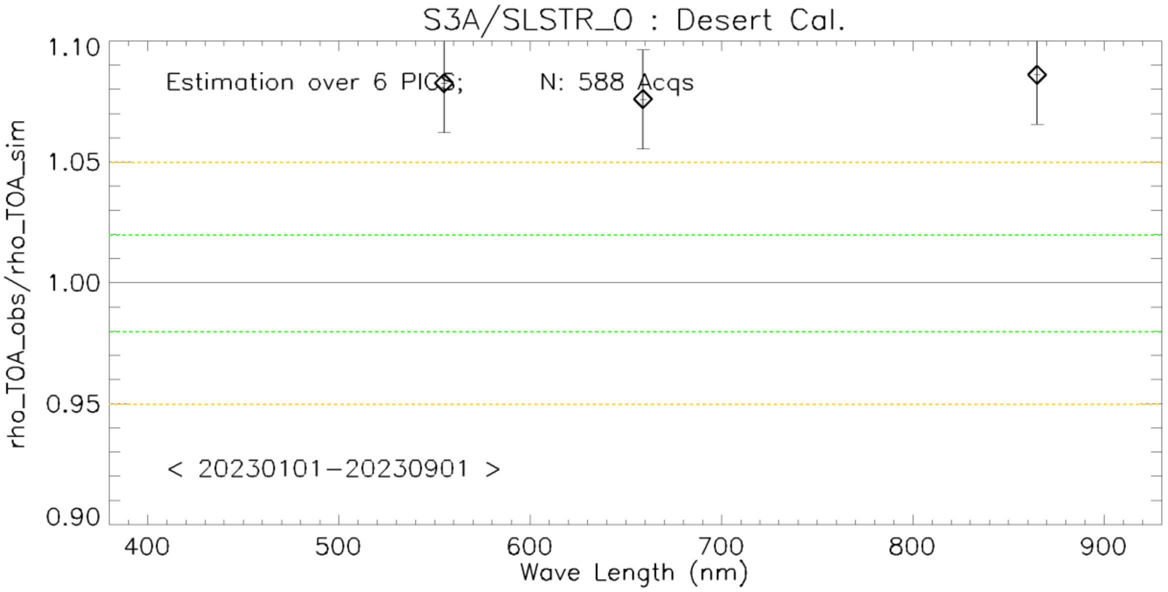
S3A/SLSTR_O : Desert Cal.
Estimation over 6 PICS; N: 588 Acqs
< 20230101–20230901 >
rho_TOA_obs/rho_TOA_sim
1.10
1.05
1.00
0.95
0.90
400
500
600
700
800
900
Wave Length (nm)

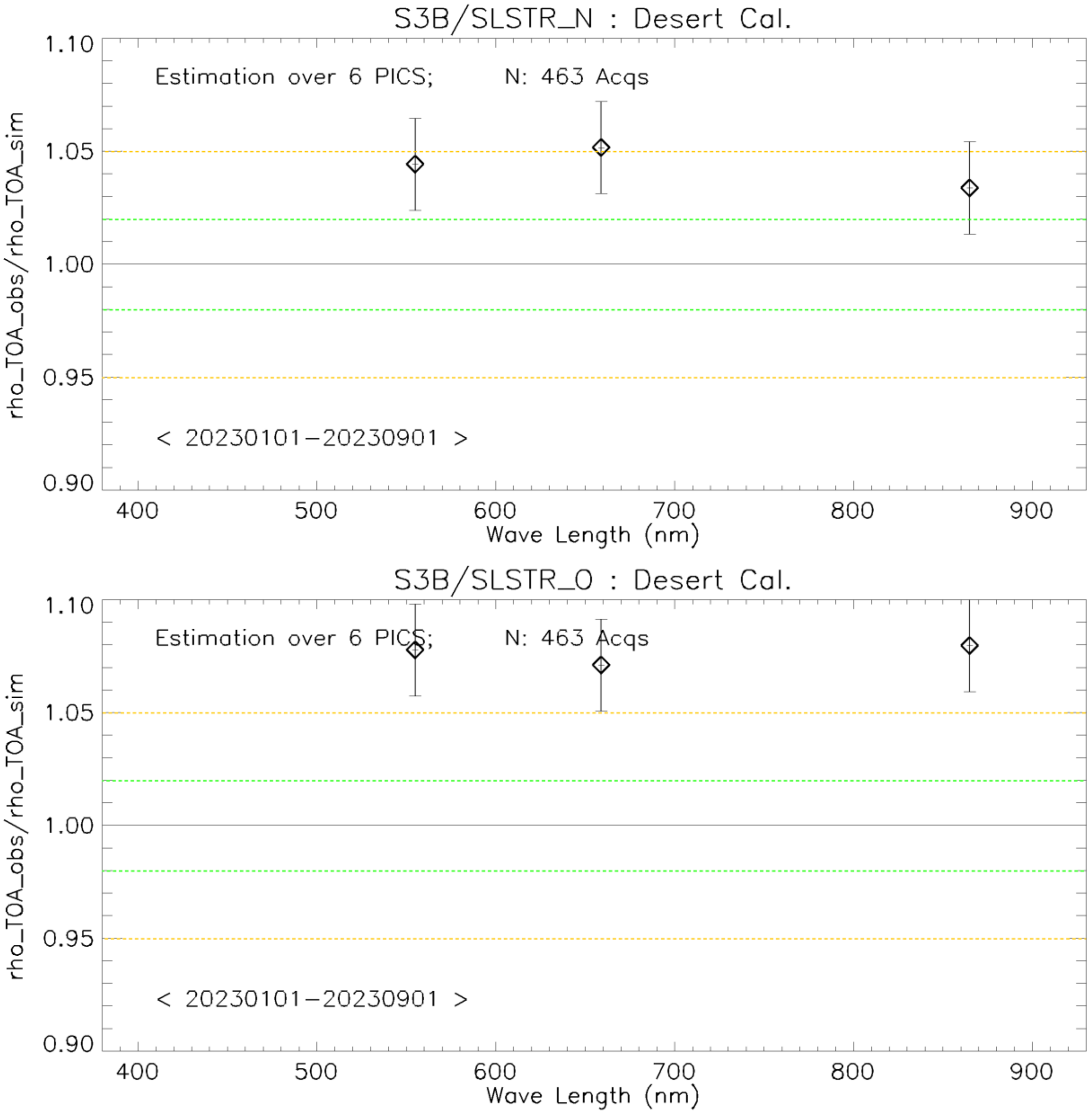

Figure 26: The estimated gain values for SLSTR-A and SLSTR-B (top to bottom) Nadir & Oblique views respectively over the 6 PICS sites identified by CEOS over the period January 2023- August 2023 as a function of wavelength. Dashed-green and orange lines indicate the 2% and 5% respectively. Error bars indicate the desert methodology uncertainty.

Validation over Rayleigh

Rayleigh method has been performed from the available mini-files over the period **January 2022-August 2023** for SLSTR-A and SLSTR-B. The gain coefficients of both sensors are consistent with the previous results (Figure 27).

Validation over Glint

Glint calibration method has been performed over the period **January 2022- August 2023** for both SLSTR-A and SLSTR-B. The gain coefficients of both sensors are consistent with the previous results over the Nadir view (Figure 27).

Validation results synthesis

The results synthesis displayed below on (Figure 27).

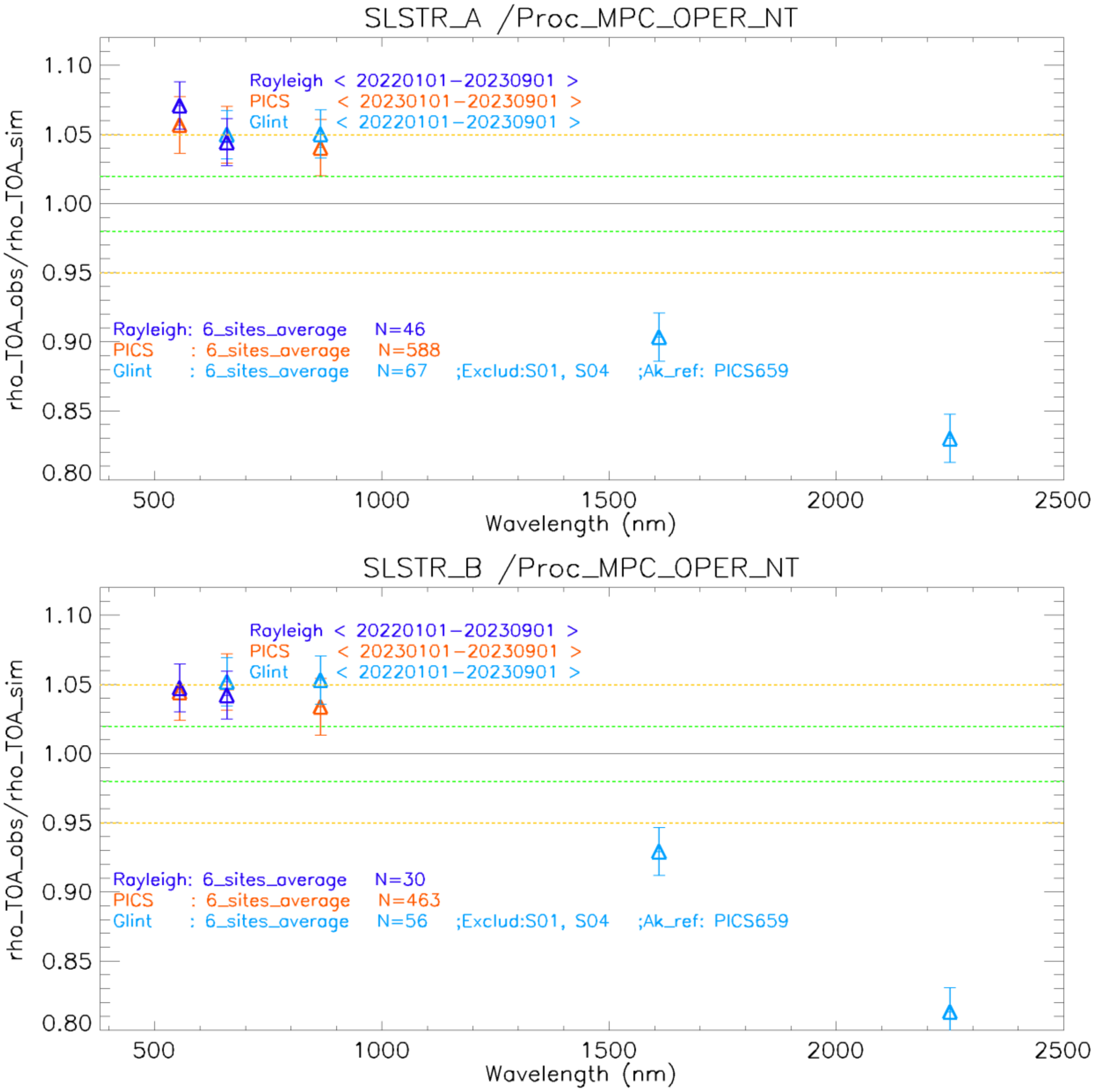

Figure 27: The estimated gain values for SLSTR-A and SLSTR-B (Nadir view) from Glint and Rayleigh methods over the period Jan 2022--August 2023 and PICS method over the period Jan 2023--August 2023 as a function of wavelength. We use the gain value of S02 from Desert-PICS method as reference gain for Glint method. Dashed-green and orange lines indicate the 2% and 5% respectively. Error bars indicate the method uncertainties.

Cross-mission Intercomparison over PICS:

X-mission Intercomparison between SLSTR-A, SLSTR-B, MERIS, MSI-A, MSI-B, OLCI-A and OLCI-B has been performed over the 6 PICS-test-sites. Figure 28 shows the estimated gain over different time-series for different sensors over PICS. The spectral bands with significant absorption of water vapor and O2 are excluded. OLCI-A, SLSTR-A and SLSTR-B seem to have higher gain wrt the other sensors of about 1-4% over VNIR spectral range.

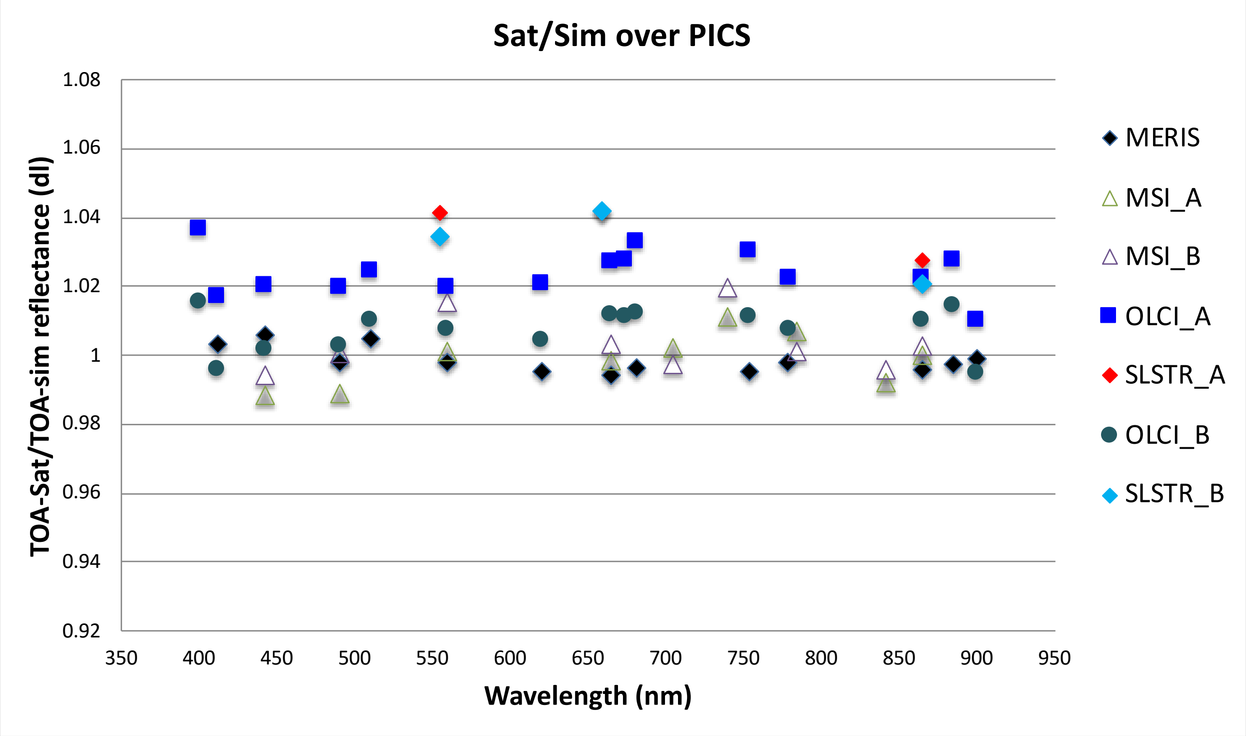

Figure 28: Ratio of observed TOA reflectance to simulated one for (black) MERIS, (pale-green) S2A/MSI, (white) S2B/MSI, (blue) S3A/OLCI, (green) S3B/OLCI, (red) S3A/SLSTR-NADIR, and (cyan) S3B/SLSTR-NADIR averaged over the six PICS test sites as a function of wavelength.

5.3 Level-1 Geometric Validation

S3_MR_1090 Geolocation accuracy: Improved geo-location accuracy is possible when using ground control points and Sentinel-3 shall be designed to ensure a geolocation accuracy of better than 0.5rm of the spatial resolution of the optical sensor when using ground control points.

S3_MR_1100 Inter channel co-registration. The inter channel spatial co-registration for Sentinel-3 visible measurements shall be < 0.5 of the spatial resolution of the sensor over the full spectral range (goal of 0.3 of the spatial resolution of the sensor)

S3_MR_1100 Inter channel co-registration: The inter channel spatial co-registration for Sentinel-3 SWIR and TIR measurements shall be sufficient to allow these channels to be co registered with visible channels at higher spatial resolution data.

Regular monitoring using the GeoCal Tool implemented at the MPC is normally carried out. On average, the geolocation accuracy of the VIS-SWIR channels meets requirements for SLSTR-A and SLSTR-B.

GeoCal is a tool that monitors the geolocation performance in Level-1 images by correlation of the images with reference features containing ground control points (GCP). Each Level-1 granule typically contains several hundred GCPs if over land, which are filtered based on signal-to-noise to obtain a daily average in the across and along track directions.

The geolocation uncertainty is stable and within requirements during the reporting period.

5.3.1 SLSTR-A

The results for August 2023 are plotted in Figure 29 for SLSTR-A, giving the average positional offsets in kilometres for Nadir and Oblique views.

GEOCAL Offsets over the last month

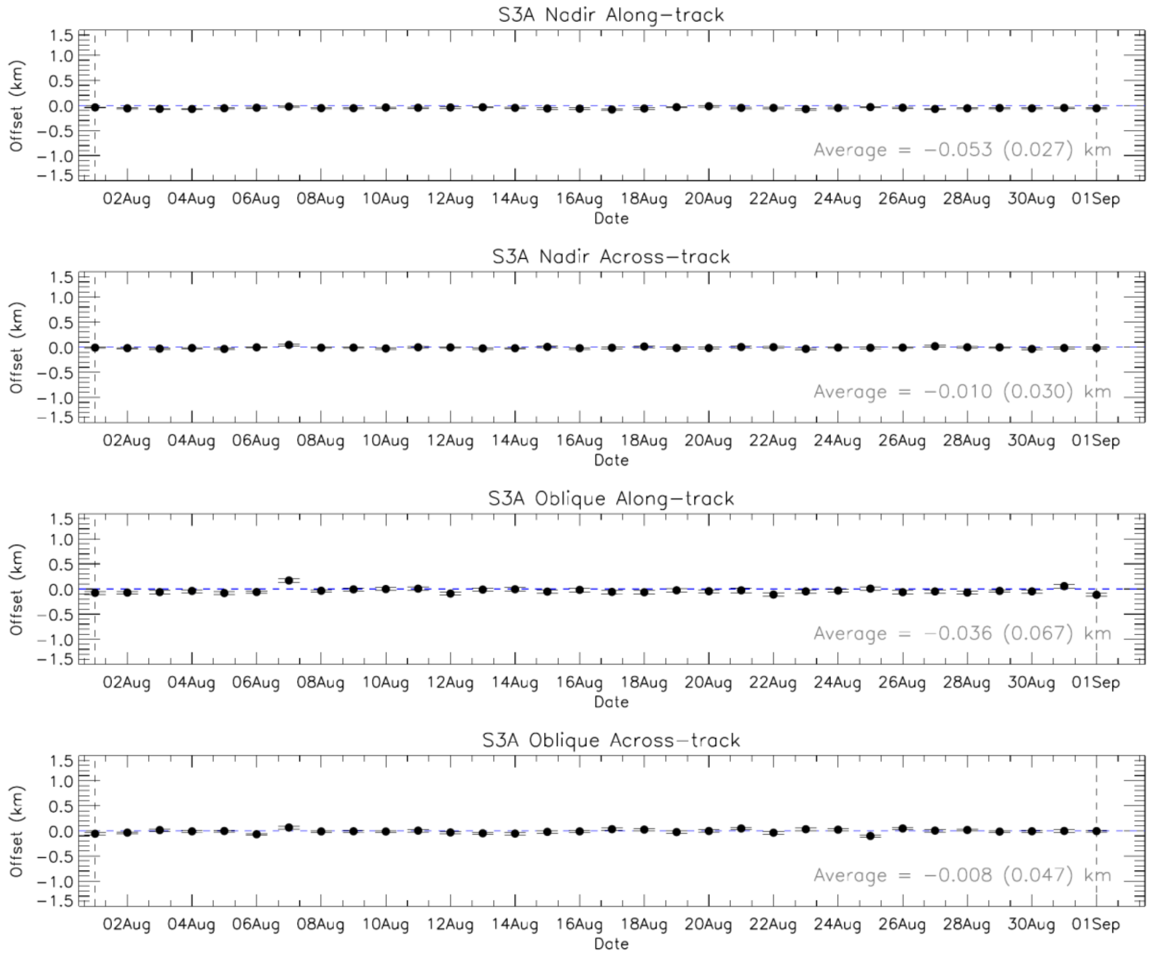

Figure 29: SLSTR-A daily offset results in km from the GeoCal Tool analysis for Nadir along- and across-track (top two plots) and Oblique along- and across-track (bottom two plots) for August 2023. The error bars show the standard deviation.

5.3.2 SLSTR-B

The results for August 2023 are plotted in Figure 30 for SLSTR-B, giving the average positional offsets in kilometres for Nadir and Oblique views.

GEOCAL Offsets over the last month

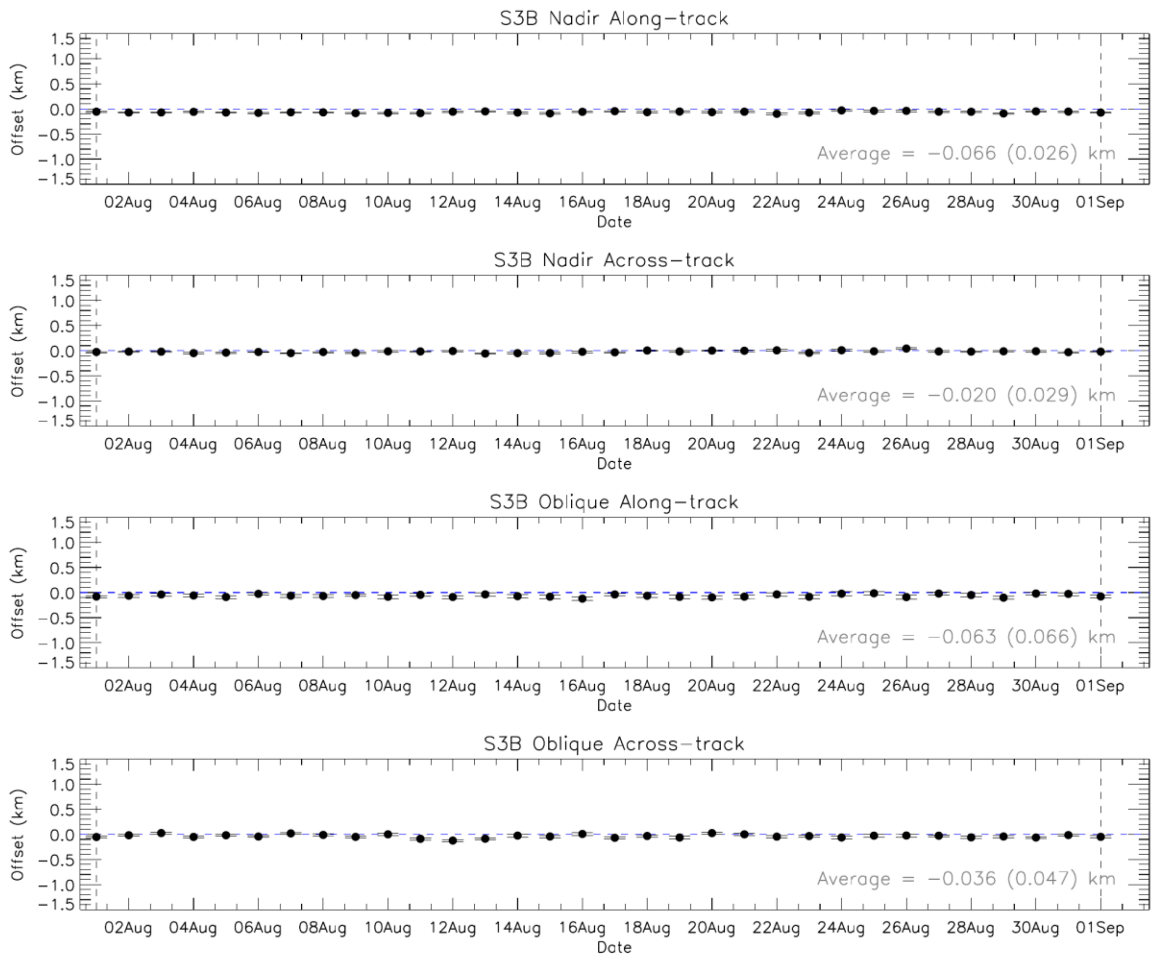

Figure 30: SLSTR-B daily offset results in km from the GeoCal Tool analysis for Nadir along- and across-track (top two plots) and Oblique along- and across-track (bottom two plots) for August 2023. The error bars show the standard deviation.

6 Level 2 LST validation

Level 2 Land Surface Temperature products have been validated against *in situ* observations (Category-A validation) from eight "Gold Standard" Stations. The different categories of validation are first described in the LST Validation Protocol (Schneider et al., 2012) and reinforced in the CEOS WGCV-LPV Land Surface Temperature Product Validation Best Practice Protocol (Guillevic et al., 2017). In all cases it is the NTC products that are validated, and the Probabilistic cloud masking implementation is used for all cloud masking. Both S3A and S3B L2 products are produced with the updated LST coefficients following the operational release on 25th February 2019. In each case the latest temporal interpolation for the probabilistic cloud mask is applied following the L1 operational release on 15th January 2020. The updated cloud coefficients ADF was applied on 23rd October 2020.

The validation results presented in this issue cover the period of **Q2 2023** (April-June).

6.1 Category-A validation

Category-A validation uses a comparison of satellite-retrieved LST with *in situ* measurements collected from radiometers sited at a number of stations spread across the Earth, for which the highest-quality validation can be achieved. Here we concentrate on twelve "Gold Standard" stations which are installed with well-calibrated instrumentation: twelve from the SURFRAD network (Bondville, Illinois; Desert Rock, Nevada; Fort Peck, Montana; Goodwin Creek, Mississippi; Penn State University, Pennsylvania; Sioux Fall, South Dakota; Table Mountain, Colorado); two from the ARM network (Southern Great Plains, Oklahoma; Barrow, Alaska); and three from the USCRN network (Williams, Arizona; Des Moines, Iowa; Manhatten, Kansas).

For the SURFRAD field pyrgeometers the uncertainty is estimated to be ±5 Wm-2 (Augustine and Dutton, 2013). For ARM, the uncertainty of the measured brightness temperatures was set to ±0.5 K for Southern Great Plains (Morris, 2006), and for North Slopes Alaska the uncertainty of the IR radiance data was set to ±4 Wm-2 (Stoffel, 2006). For the USCRN network, which uses Apogee SI-121s the uncertainty is set as the manufacturers estimate of ±0.2 K.

The results can be summarised as follows (accuracy is used as the metric rather than uncertainty as this is then a straight comparison with mission requirements):

Table 10: Average absolute accuracy in K of the SL_2_LST product with respect to Gold Standard stations for Q2 2023.

Satellite	Day	Night
S3A	1.4	0.6
S3B	1.4	0.5

For both SLSTR-A and SLSTR-B both the daytime and night-time absolute accuracies (which are derived from the absolute values of all the mean biases from the individual stations) are close to the mission requirement of 1K. The main impact on accuracy and precision is driven by any errors in the cloud masking.

SLSTR-A	**SLSTR-B**
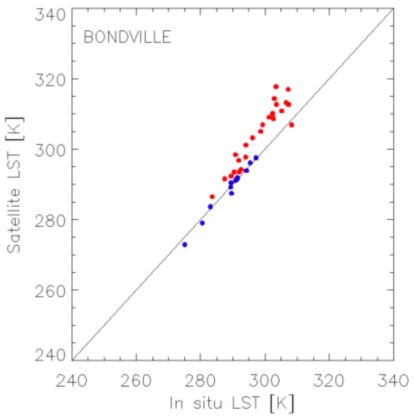	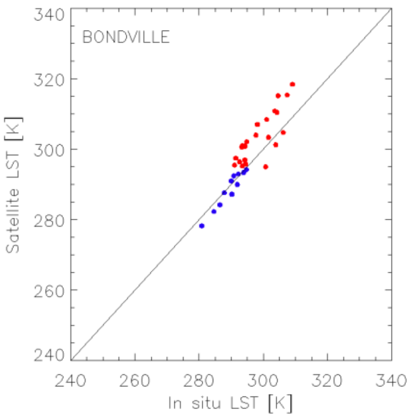
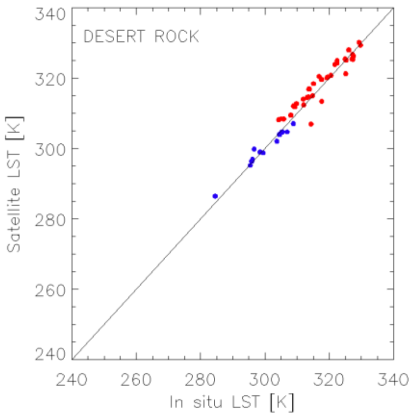	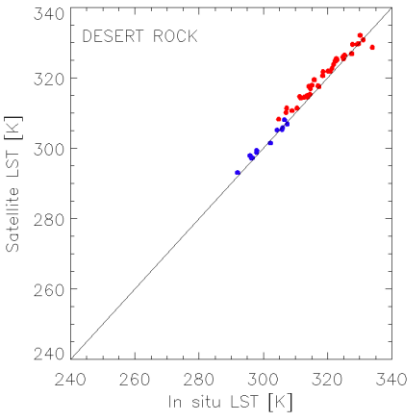
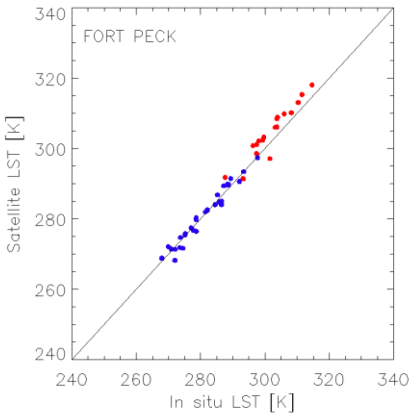	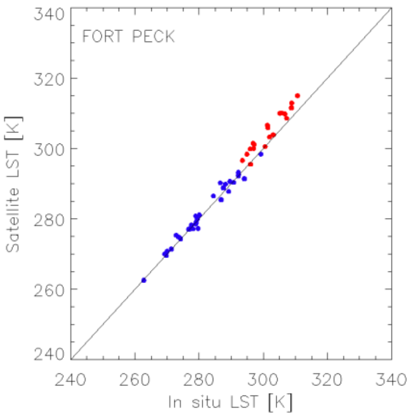

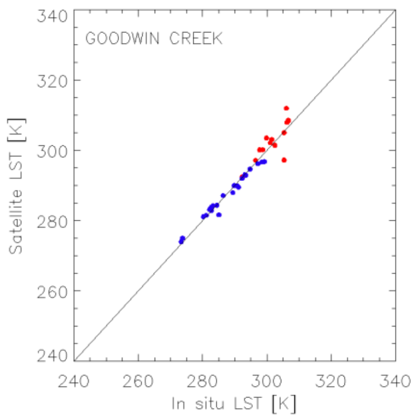
GOODWIN CREEK
Satellite LST [K]
In situ LST [K]
240
260
280
300
320
340

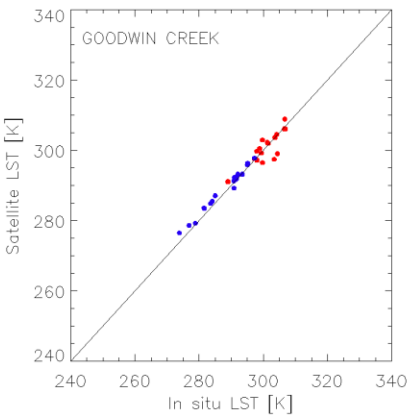
GOODWIN CREEK
Satellite LST [K]
In situ LST [K]
240
260
280
300
320
340

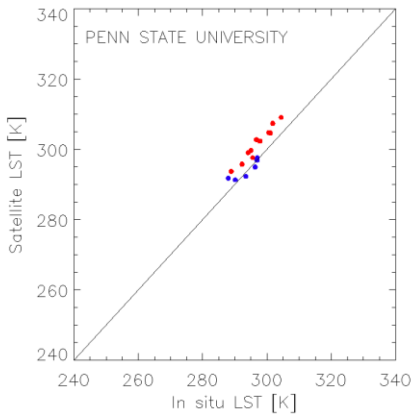
PENN STATE UNIVERSITY
Satellite LST [K]
In situ LST [K]
240
260
280
300
320
340

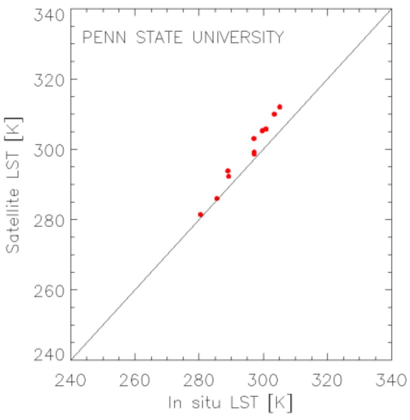
PENN STATE UNIVERSITY
Satellite LST [K]
In situ LST [K]
240
260
280
300
320
340

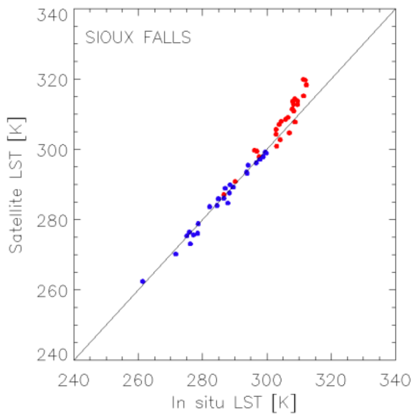
SIOUX FALLS
Satellite LST [K]
In situ LST [K]
240
260
280
300
320
340

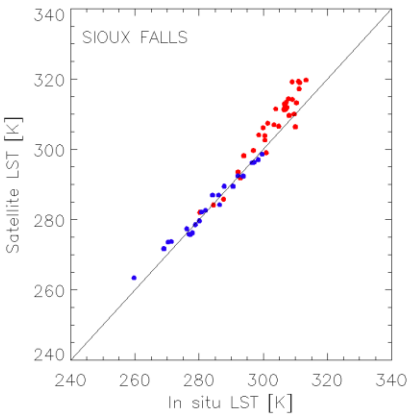
SIOUX FALLS
Satellite LST [K]
In situ LST [K]
240
260
280
300
320
340

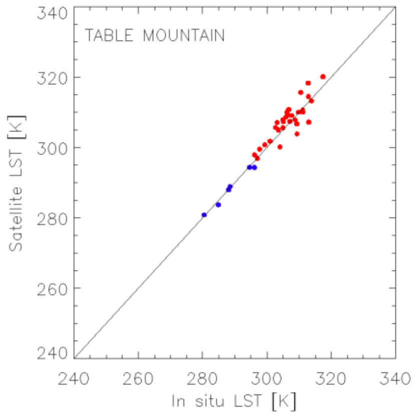

TABLE MOUNTAIN
Satellite LST [K]
In situ LST [K]
240
260
280
300
320
340

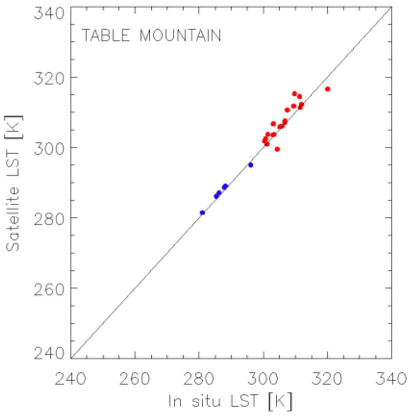

TABLE MOUNTAIN
Satellite LST [K]
In situ LST [K]
240
260
280
300
320
340

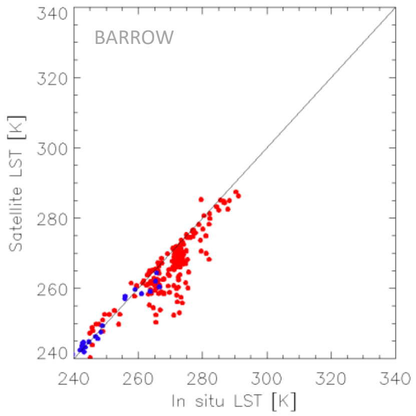

BARROW
Satellite LST [K]
In situ LST [K]
240
260
280
300
320
340

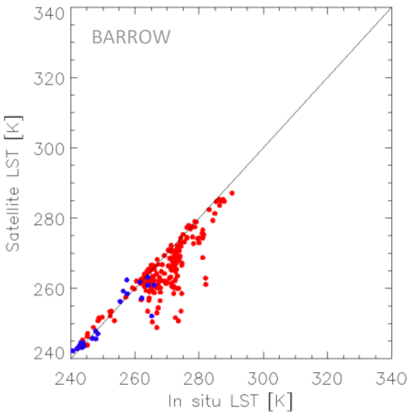

BARROW
Satellite LST [K]
In situ LST [K]
240
260
280
300
320
340

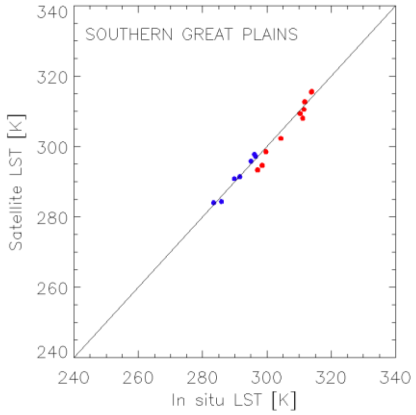

SOUTHERN GREAT PLAINS
Satellite LST [K]
In situ LST [K]
240
260
280
300
320
340

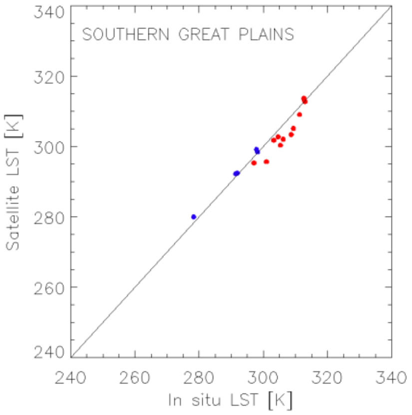

SOUTHERN GREAT PLAINS
Satellite LST [K]
In situ LST [K]
240
260
280
300
320
340

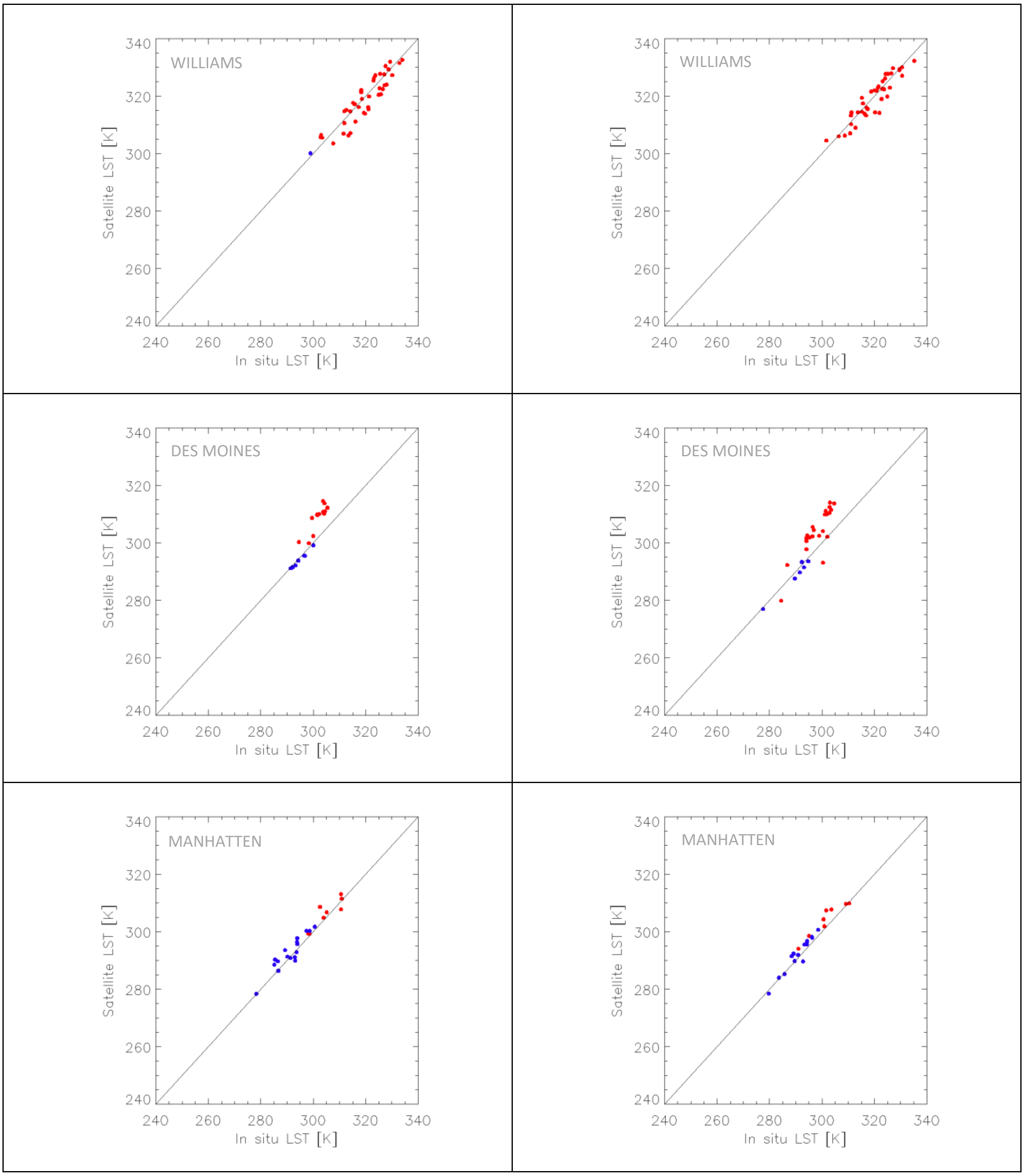

Figure 31: Validation of the SL_2_LST product in Q2 2023 for SLSTR-A (left) and SLSTR-B (right) at twelve Gold Standard in situ stations of the SURFRAD network plus two Gold Standard station from the ARM network. The matchups are split between daytime (red) and night-time (blue).

As with past cycles cloud has reduced the number of matchups per station to single figures for most stations during day or night, with some missing statistics entirely. It is therefore challenging to determine robust statistics. The cumulative statistics are presented in each Annual Report. Nonetheless, it can be seen that overall, the matchups are in general close to the 1:1 line with few outliers. There is a small systematic bias evident during daytime at some stations, which may indicate an update to the retrieval coefficients may be worth exploring. Some cloud over-masking (night-time) and under-masking (daytime) appears for some of the sites and may be worth exploring whether the cloud coefficients need further fine tuning.

6.2 Category-C validation

Category-C validation uses inter-comparisons with similar LST products from other sources such as other satellite sensors, which give important quality information with respect to spatial patterns in LST deviations. Here we compare the SL_2_LST product from both SLSTR-A and SLSTR-B with the operational SEVIRI L2 product available from the LSA SAF. The typical uncertainty of the SEVIRI L2 product ranges between ~1 K over much of Africa and ~3 K over the deserts. The results can be summarised:

Table 11: Median differences in K from the intercomparison of the SL_2_LST product with respect to the operational LSA SAF SEVIRI LST product for December 2022

Continent	SLSTR-A		SLSTR-B	
	Day	Night	Day	Night
Africa	-0.1	-0.1	-0.1	-0.1
Europe	1.1	1.3	1.2	1.3

For both Africa and Europe, the median differences across the continent for both SLSTR-A and SLSTR-B are relatively small, with very few locations with larger differences. The median is used to minimise the impact of any outliers. This is the same for both SLSTR-A and SLSTR-B and is primarily driven by differences in viewing geometry between the SLSTR instruments and SEVIRI and is expected, and in agreement with previous studies of polar orbiting matchups with SEVIRI (Ghent et al., 2017; Trigo et al., 2008). Eastern matchups (such as over the Arabian Peninsula and north-eastern Europe) are towards the edge of the SEVIRI disk and therefore represent large viewing angles. At these extreme viewing angles it is expected that SLSTR LST would be increasingly higher than SEVIRI LST, and the SEVIRI uncertainty increases above 3 K at these extreme angles. For both daytime and night-time the differences are mainly < 1K for Africa for both SLSTR-A and SLSTR-B. During daytime differences are over 1K for Europe as a result of increasing differences due to geometry as days get warmer. Differences are not the same as previous cycles for both Europe and Africa which may indicate responses due to changing seasons.

Other analysis can be summarised as follows:

- Differences with respect to biomes tend to be larger during the day for surfaces with more heterogeneity and/or higher solar insolation
- Differences increase for both day and night towards the edge of the SEVIRI disk as the SEVIRI zenith angles become larger

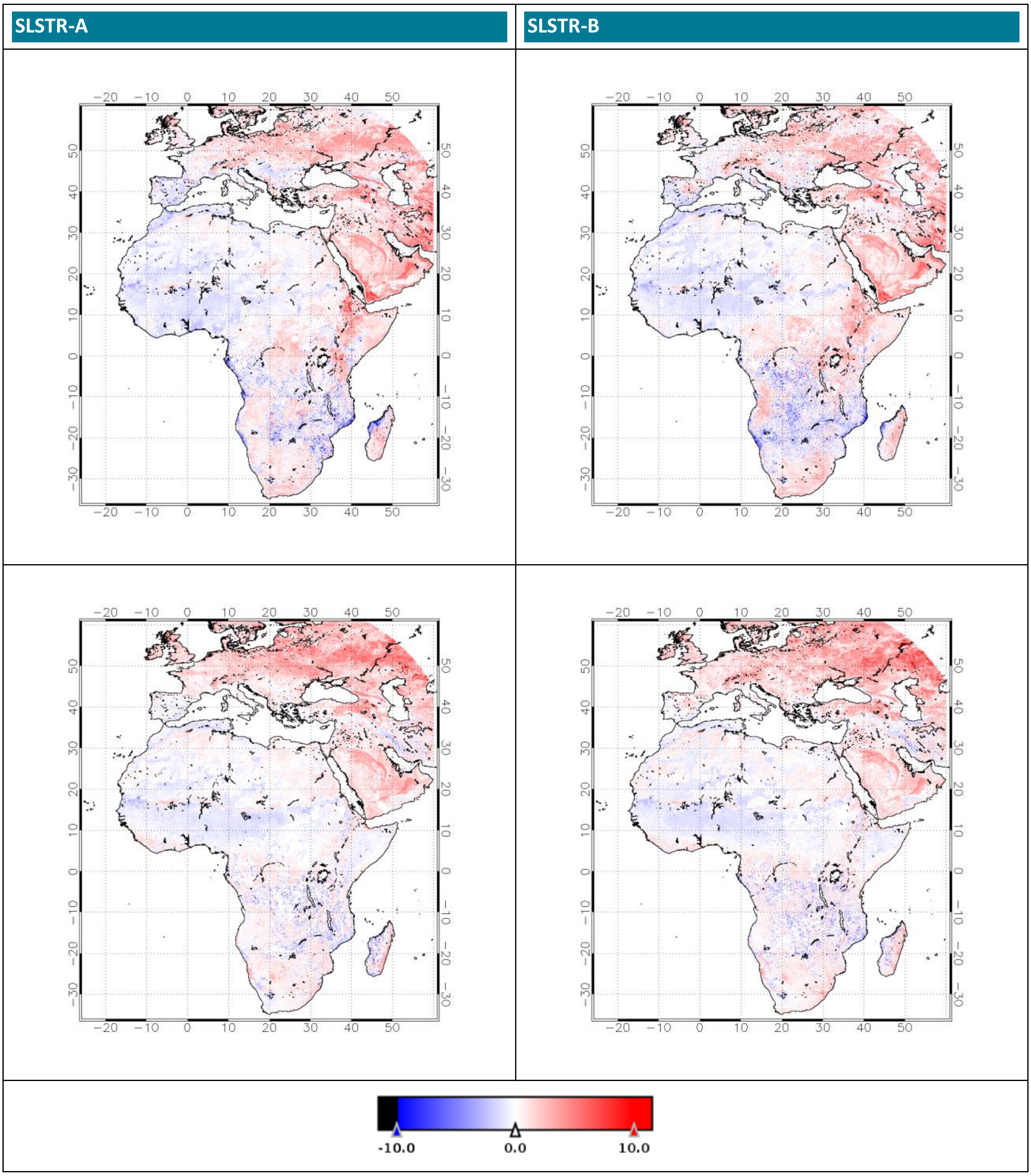

Figure 32: Intercomparison of the SL_2_LST product with respect to the operational LSA SAF SEVIRI LST product for December 2022 for SLSTR-A (left) and SLSTR-B (right). Daytime composites are in the top row and Night-time composites are in the bottom row.

While some of these differences are > 1 K they are all within the corresponding uncertainty of SEVIRI at the pixel-scale (> 2K), and so the **two products can be assessed as being consistent**.

6.3 Level-3C Assessment

To better understand the global product and identify any gross issues Level-3 evaluation is also performed. Here we generate monthly daytime and night-time 0.05° composites of the LST field and corresponding sampling ratios. The sampling ratios are derived as clear_pixels / (clear_pixels + cloudy_pixels).

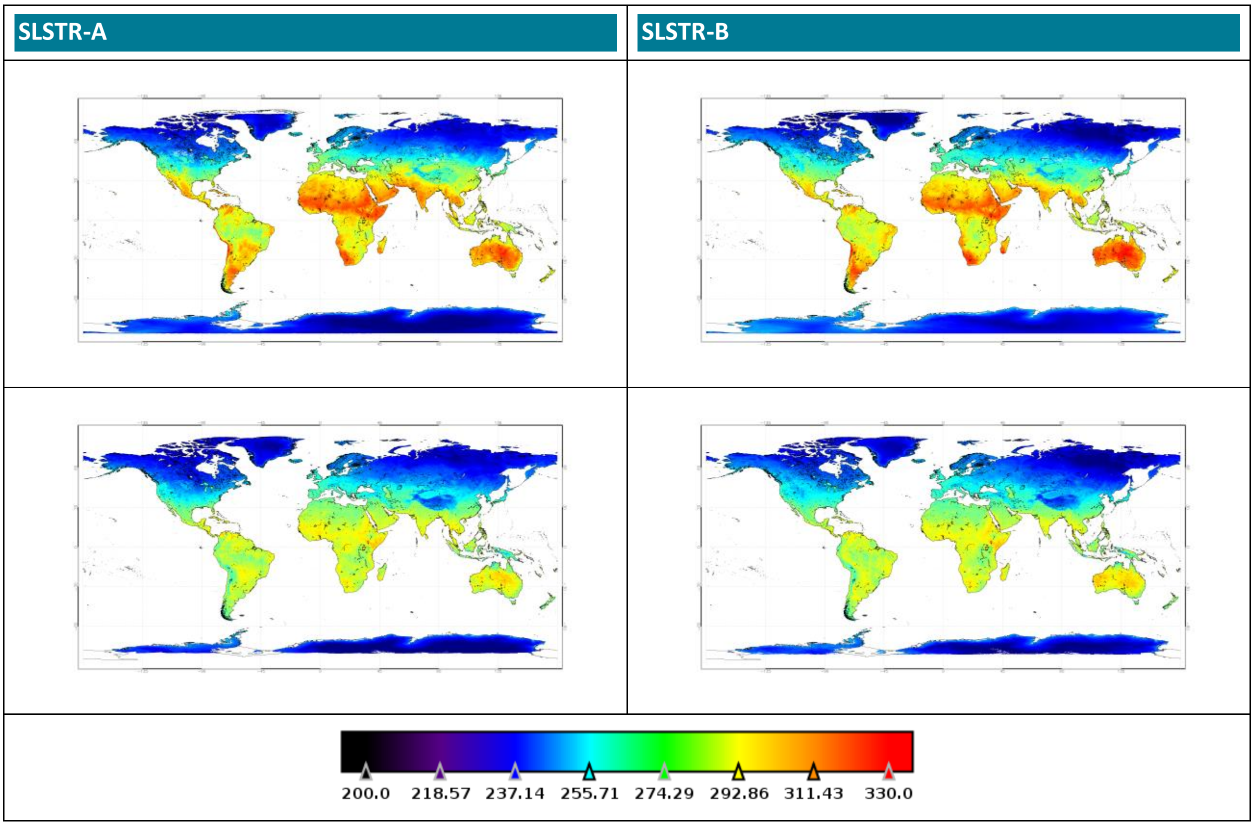

Figure 33: Monthly composites at 0.05° of LST for December 2022 for SLSTR-A (left) and SLSTR-B (right). Daytime composites are in the top row and Night-time composites are in the bottom row.

6.4 References

Augustine, J.A. and Dutton, E.G. (2013). Variability of the surface radiation budget over the United States from 1996 through 2011 from high-quality measurements. Journal of Geophysical Research: Atmospheres 118, 43–53.

Ghent, D. J., Corlett, G. K., Göttsche, F.-M., & Remedios, J. J. (2017). Global land surface temperature from the Along-Track Scanning Radiometers. Journal of Geophysical Research: Atmospheres, 122. https://doi.org/10.1002/2017JD027161

Guillevic, P., Göttsche, F., Nickeson, J., Hulley, G., Ghent, D., Yu, Y., Trigo, I., Hook, S., Sobrino, J.A., Remedios, J., Román, M. & Camacho, F. (2017). Land Surface Temperature Product Validation Best Practice Protocol. Version 1.0. In P. Guillevic, F. Göttsche, J. Nickeson & M. Román (Eds.), Best Practice for Satellite-Derived Land Product Validation (p. 60): Land Product Validation Subgroup (WGCV/CEOS), doi:10.5067/doc/ceoswgcv/lpv/lst.001

Morris, V.R. Infrared Thermometer (IRT) Handbook (ARM TR-015) (2006). Technical report, Atmospheric Radiation Measurement, Climate Research Facility, U. S. Department of Energy.

Schneider, P., Ghent, D., Corlett, G., Prata, F., and Remedies, J. (2012). AATSR validation: LST validation protocol. Internal publication, UL-NILU-ESA-LST-LVP Issue 1 Revision 0, page 1-39. http://lst.nilu.no/Portals/73/Docs/Reports/UL-NILU-ESA-LST-LVP-Issue1-Rev0-1604212.pdf.

Stoffel, T. Ground Radiation (GNDRAD) Handbook (ARM TR-027) (2006). Technical report, Atmospheric Radiation Measurement, Climate Research Facility, U. S. Department of Energy.

Trigo, I. F., Monteiro, I. T., Olesen, F., & Kabsch, E. (2008). An assessment of remotely sensed land surface temperature. Journal of Geophysical Research, 113(D17), D17108. https://doi.org/10.1029/2008JD010035

7 Level 2 FRP validation

7.1 The SLSTR Fire Radiative Power product

The SLSTR FRP NTC product (both SLSTR-A and SLSTR-B) has been released to the public on August 19th, 2020. The current processing baseline for SLSTR-A and SLSTR-B FRP products is FRP_NTC.004.07.00 and was deployed in the Land processing centres on February 28th, 2022, for both SLSTR-A and for SLSTR-B. This baseline is including an updated FRP algorithm, called FRP V2. This updated algorithm is based on the previous one, with a similar nighttime algorithm, but includes improved thermal fire detection over daytime products. Daytime detection is performed using a mixed thermal band. The S7 brightness temperature is considered by default for all pixels. In the event of saturation, the F1 channel is used instead for the saturated pixel, and all pixels around it in a 11 x 11 pixels window that either have a S7 brightness temperature above 300 K, or a brightness temperature difference between S7 and S8 higher than 10 K. AF detection during nighttime remains similar to that of the FRP V1 algorithm and uses the F1 measurements. The FRP V2 algorithm also introduced an alternative fire detection using SWIR channels, however this functionality is not yet part of the validation report.

This report only focuses on measurements obtained from the thermal channels using the FRP V2 algorithm over the months of April, May, and June. First, the fires detected during nighttime are assessed. Then, the same analysis is repeated for daytime fires.

7.2 Validation methodology

Validation of the SLSTR L2 FRP products can be performed using either in-situ data such as airborne measurements or using products from a reference satellite for inter-comparison. Active fires in situ data are unfortunately not frequent enough to validate fire satellite data products on an operational basis. The current comparison methodology uses products from NASA Moderate-Resolution Imaging Spectroradiometer (MODIS) as reference fire data for the intercomparisons.

This present inter-comparison, initially based on previous work from M. Wooster and W. Xu on the FRP Prototype and on the evaluation of SEVIRI fire data, aims to assess two things:

1. The detection of fires' position and extent in time and space.

2. The estimated radiative fire power (FRP) of active fires.

To do so, the SL_2_FRP product from SLSTR-A and SLSTR-B are compared with the operational MODIS MOD14 FRP product from MODIS Terra. This inter-comparison should not be interpreted as a full validation exercise but rather as a check of the consistency of the FRP products derived from the satellites, as ground truth is not available.

The methodology to obtain data fit for comparison purposes is outlined hereafter:

- Once areas of interest have been defined, identify all SL_2_FRP scenes containing active fires;
- Download MODIS MOD14 data with a scene overpass time within ± 6 minutes from that of SLSTR;
- Restrict observations to a scan angle of ±30° or equivalent pixel area of 1.7 km^2 to avoid edge-of-swath data, and to the common area of detection between the two products;
- Reproject MODIS pixels on the SLSTR F1 grid. If multiple MODIS active fire pixels (AFP) are present in the same equivalent SLSTR grid cell, their combined FRP is used.

Omissions, commissions, and double detections are then evaluated. A fire is classified as omitted if no SLSTR fire pixel is present in a 7 x 7 pixels window around a MODIS fire pixel. Conversely, a fire is classified as commissioned if no MODIS fire pixel is present in a 7 x 7 pixels window around a SLSTR fire pixel. If SLSTR and MODIS pixels are present within the windows, the fire is classified as double detected.

The FRP analysis is twofold: it is done both at the pixel level, and at the cluster level. A cluster is defined as fires close enough to be interpreted as a single fire event (i.e. the detected fire pixels are next to one another). In both cases, as MODIS FRP data is provided before atmospheric correction, they are atmospherically corrected using the water vapor content estimated by Sentinel 3 as the basis to compute the transmission.

The detected fire clustering is done according to the following procedure: for both sensors, a connected-component labeling using an 8-connectivity is used to label clusters. Then, iteratively, clusters from one satellite having an overlap with clusters from the other are merged to form superclusters, until each supercluster from one satellite only overlaps with a single supercluster from the other. Figure 34 illustrates the process. Finally, superclusters associated with problematic flags (clouds/water/detection/high S7-S8 difference) are removed from the datasets. The remaining matching pairs of SLSTR and MODIS superclusters are used for further analysis regarding FRP estimates.

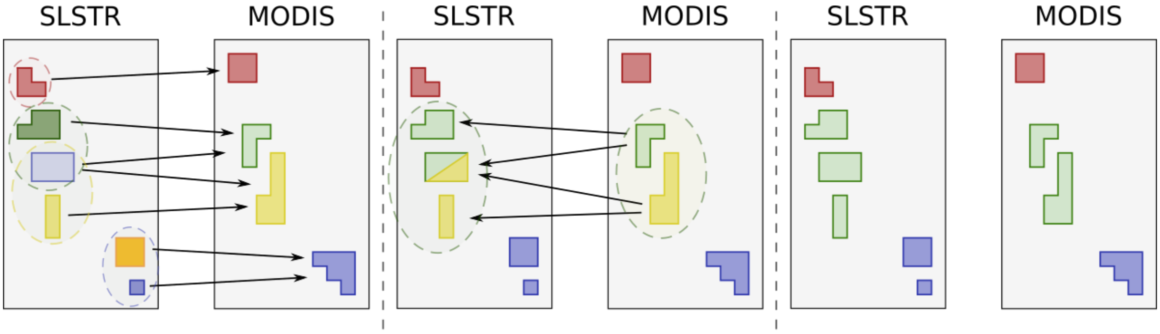

Figure 34: Formation process of the pairs of superclusters depending on AFP detected each satellite. Fire clusters and superclusters are identified by their colors. At the end of the process, pairs of SLSTR and MODIS superclusters share the same color.

South America, Central Africa, and Australia (see Figure 35). Since the last report, the SLSTR pixel grid was updated to take into account the geometric alignment between VNIR and thermal bands, and the algorithm used to reproject MODIS pixels on the SLSTR grid was refined Finally, the clustering algorithm was updated to better aggregate clusters in the event superclusters generated from one satellite are associated to the same supercluster from the other.

.

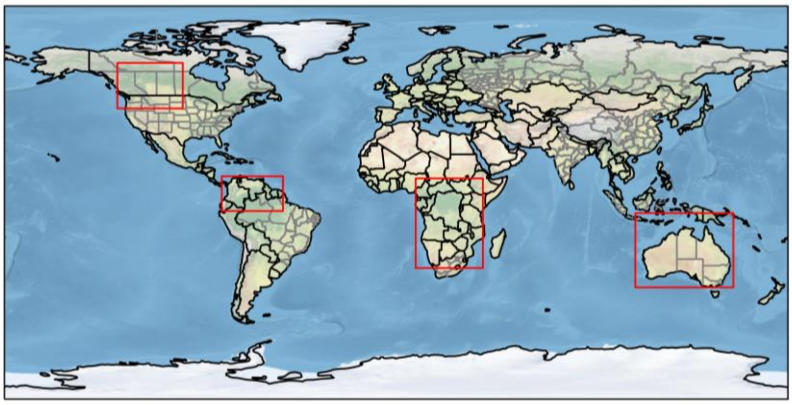

Figure 35: Selected zones for the intercomparison over the April-June 2023 period

7.3 Results

7.3.1 Global distributions of the fires

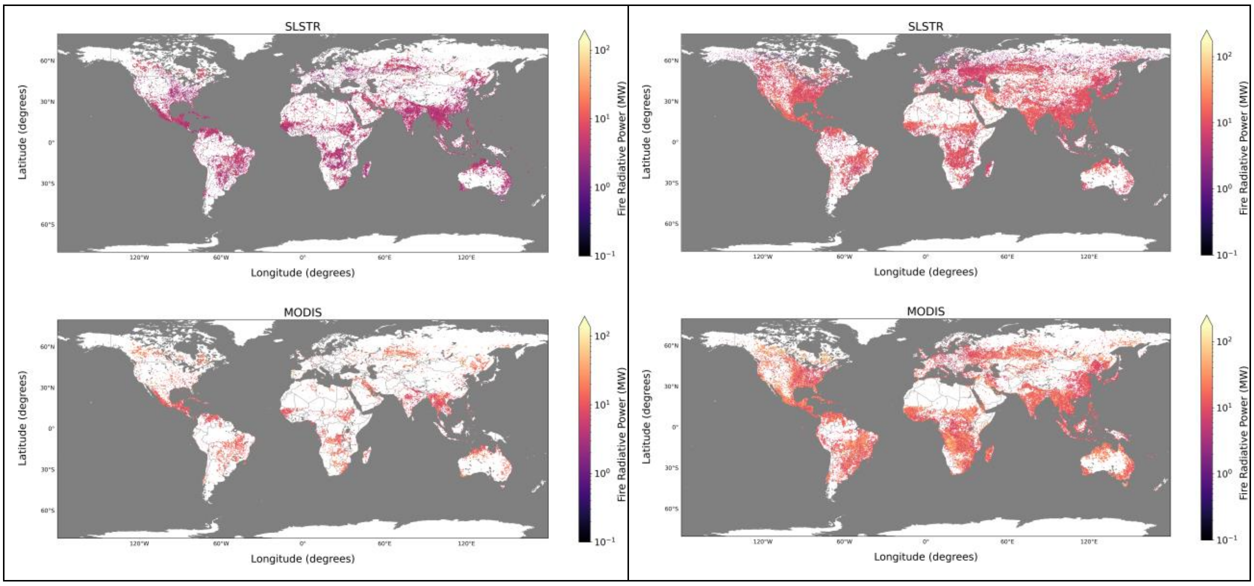

Figure 36: : Fires detected by SLSTR and MODIS at nightime (left) and daytime (right).

Figure 36 shows the location and radiative power of fires detected by SLSTR and MODIS during night and daytime. On one hand, SLSTR seems to be detecting more fire than MODIS during nighttime, most of them having a lower intensity, while there are few omissions. On the other hand, during daytime, omissions seem to be much more frequent, especially in the southern hemisphere, with large swathes of Brazil, southern Africa, and Australia presenting MODIS fires when no fire was detected by SLSTR.

7.3.2 Nighttime Fires Validation

Table 12 presents a summary of the intercomparison between active fires detected by SLSTR and MODIS over the April—June 2023 period, as well as past periods. Similarly, to previous periods, the data present a significantly larger quantity of commissions (about half of SLSTR-detected fires are commissions) compared to the omissions. Conversely, omissions are down from previous periods, with only 3% of MODIS-detected fires not being detected by SLSTR, down from 14% during the January—March period. The FRP distributions of both MODIS and SLSTR clusters are both significantly higher than past periods, with increased total, mean, and median values (Total SLSTR FRP for April—June 2023 is 157,689 MW, up from 70,529 MW the previous three months): more intense fires occurred over the present period and study area than in the previous ones.

Table 12: Summary of the intercomparison between nighttime SLSTR and MODIS active fires over the April—June 2023 period. Results from previous 3-months comparisons are included for information purposes.

Variable	Value			
	Apr.—Jun. 2023	Jan.—Mar. 2023	Oct.—Dec. 2022	Jul.—Sep. 2022
Commissions (% of total SLSTR AFP)	9,380 (49%)	15,149 (56.3%)	13,093 (55.1%)	20,092 (62.3%)
Omissions (% of total MODIS AFP)	99 (3%)	567 (14%)	694 (17%)	883 (18%)
FRP of commissions (MW)	78,860	37,392	40,359	58,380
FRP of omissions (MW)	1,212	14,459	30,641	34,123
SLSTR AFP double detec. (% of total SLSTR AFP)	9,885 (51%)	11,762 (43.7%)	10,665 (44.9%)	12,147 (37.7%)
MODIS AFP double detec. (% of total MODIS AFP)	3,224 (97%)	3,481 (86.0%)	3,341 (82.8%)	4,089 (82.1%)
Total SLSTR AFP	19,265	26,911	23,758	32,239
Total MODIS AFP	3,323	4,048	4,035	4,972
Mean number of SLSTR AFP per cluster	11.9	6.4	6.4	5.9
Total FRP of SLSTR clusters (MW)	157,689	70,529	81,672	95,704
Mean SLSTR FRP per cluster (MW)	209,1	41.2	54.0	50.4
Median SLSTR FRP per cluster (MW)	34,3	18.9	21.0	21.7
Mean number of MODIS AFP per cluster	3,9	1.8	1.9	1.9
Total FRP of MODIS clusters (MW)	202,057	58,894	70,530	85,814
Mean MODIS FRP per cluster (MW)	268.0	34.8	46.7	45.2
Median MODIS FRP per cluster (MW)	23.2	11.7	13.6	14.3
Mean bias of FRP per cluster (MW)	-58.8	6.9	7.4	5.2
Median of FRP scatter per cluster (MW)	7.5	5.0	6.0	5.2
RMSD of FRP per cluster (MW)	697.2	48	59	71
Percentiles 25, 75 of SLSTR clusters FRP (MW)	10.0, 60.8	10.6, 34.8	12.1, 40.2	12.1, 42.6
Percentiles 25, 75 of MODIS clusters FRP (MW)	17.1, 78.8	7.2, 23.3	7.8, 29.5	8.1, 31.2

As visible in Figure 37, a large proportion of the fire pixels SLSTR detects present a very low FRP (< 4 MW). Conversely, all but one fire pixel detected by MODIS had a FRP above 4 MW. The distribution of FRP above 20 MW seem to follow the same trend for both SLSTR and MODIS, indicating that the most powerful fires are detected by both satellites. The distribution of the FRP of commission pixels confirms that almost all commissions concern fires with very low FRP, highlighting the fact that SLSTR is much more sensitive than MODIS to detect active fires. Omissions, on the other hand, concern fires of very common intensities (~10 MW).

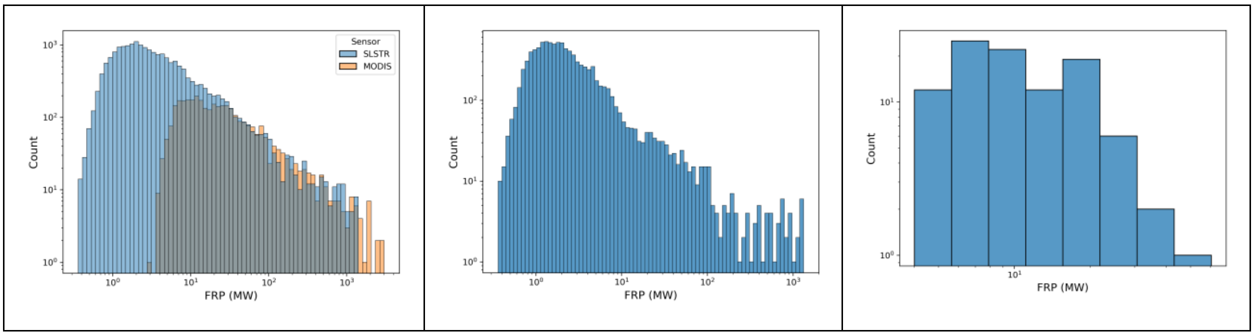

Figure 37: From left to right, for nighttime: histograms of the FRP of fires detected by SLSTR and MODIS, histogram of the FRP of commissions, histogram of the FRP of omissions.

Figure 38 shows that there is a good agreement between the FRP of clusters detected by MODIS and those detected by SLSTR when they are on the lower end. However, for very powerful fires (>3000 MW), the supercluster FRP estimated by SLSTR can be much lower than that estimated from MODIS. Indeed, it appears that the FRP relationship follows a power-law with an exponent above 1. As there are no omissions with a very high FRP, and very few omissions in general, it seems that for the high-intensity-fire pixels, MODIS estimates much higher FRP values.

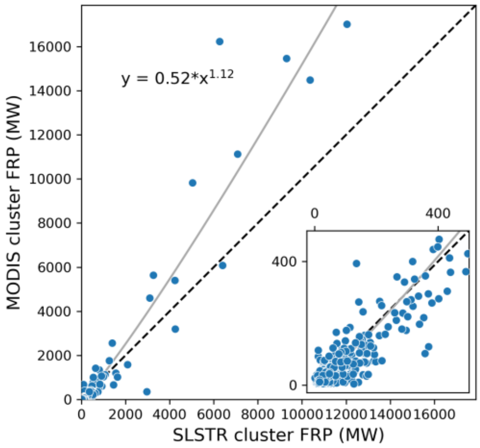

Figure 38: Comparison between the FRP of cluster pairs detected by SLSTR and MODIS during nighttime. A zoom-in is provided on the right-hand side to better see the general behaviour.

7.3.3 Daytime Fires Validation

Table 13 presents a summary of the intercomparison between active fires detected by SLSTR and MODIS over the April—June 2023 period, as well as past periods. The proportion of commissioned fire pixel seem in line with previous periods, while the proportion of omissions is significantly lower (down to 27% from ~45%). Here again, the FRP distributions of both MODIS and SLSTR clusters are both significantly higher than past periods, with increased total, mean, and median values (Total SLSTR FRP for April—June 2023 is 460,979 MW, up from 212,125 MW the previous three months), while the total quantities of AFP have not increased significantly for SLSTR, and decreased for MODIS. This highlights that fires much more intense than usual were detected by the satellites.

Table 13: Summary of the intercomparison between daytime SLSTR and MODIS active fires over the April—June 2023 period. Results from previous 3-months comparisons are included for information purposes.

Variable	Value			
	Apr.—Jun. 2023	Jan.—Mar. 2023	Oct.—Dec. 2022	Jul.—Sep. 2022
Commissions (% of total SLSTR AFP)	6,913 (31%)	4,326 (27%)	5,344 (48%)	7,613 (49%)
Omissions (% of total MODIS AFP)	2917 (27%)	6,226 (42%)	3,693 (46%)	5,720 (49%)
FRP of commissions (MW)	99,070	56,702	67,342	96,572
FRP of omissions (MW)	47,664	218,462	146,446	191,942
SLSTR AFP double detec. (% of total SLSTR AFP)	15,156 (69%)	11,931 (73%)	5,819 (52%)	8,054 (51%)
MODIS AFP double detec. (% of total MODIS AFP)	8,013 (73%)	8,720 (58%)	4,421 (54%)	5,845 (51%)
Total SLSTR AFP	22,069	16,257	11,163	15,667
Total MODIS AFP	10,930	14,946	8,114	11,565
Mean number of SLSTR AFP per cluster	6.0	2.8	2.5	2.7
Total FRP of SLSTR clusters (MW)	460,979	212,125	73,916	156,059
Mean SLSTR FRP per cluster (MW)	198.0	55.5	48.0	59.0
Median SLSTR FRP per cluster (MW)	37.4	26.9	27.4	27.4
Mean number of MODIS AFP per cluster	3.0	1.8	1.7	1.8
Total FRP of MODIS clusters (MW)	490,387	190,612	68,320	143,963
Mean MODIS FRP per cluster (MW)	211.0	49.9	44.3	54.4
Median MODIS FRP per cluster (MW)	34.8	21.5	22.3	22.5
Mean bias of FRP per cluster (MW)	-12.7	5.6	3.6	4.6
Median of FRP scatter per cluster (MW)	3.4	3.9	3.7	3.4
RMSD of FRP per cluster (MW)	375.2	67.3	58.9	64.0
Percentiles 25, 75 of SLSTR clusters FRP (MW)	16.7, 89.5	15.4, 51.4	17.0, 52.0	16.0, 54.4
Percentiles 25, 75 of MODIS clusters FRP (MW)	19.2, 90.8	11.9, 45.8	13.0, 42.9	13.5, 50.4

Figure 39 is the equivalent to Figure 38, but for daytime. The same patterns are observed: a large proportion of the fire pixels SLSTR detects present a very low FRP (< 4 MW), unlike MODIS. Again, distribution of FRP above 20 MW seem to follow the same trend for both SLSTR and MODIS, although here again MODIS estimates much higher FRP (the tail of the distribution is longer). In a similar fashion as for nighttime, commissions almost exclusively present very low FRP values, while omissions are, for the most part, average-intensity fires.

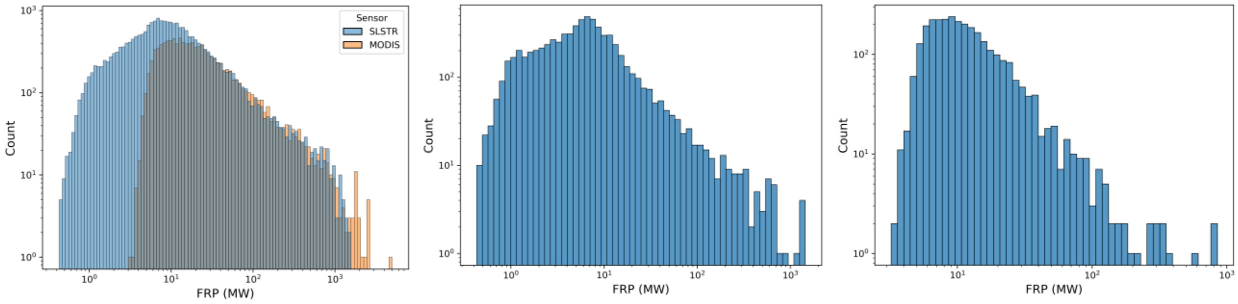

Figure 39: From left to right, for daytime: histograms of the FRP of fires detected by SLSTR and MODIS, histogram of the FRP of commissions, histogram of the FRP of omissions.

Figure 40 shows that daytime and nighttime cluster have, in general, the same patterns, with the FRP values of SLSTR clusters being generally in line with those of MODIS. However, there again, MODIS estimated FRP values tend to be higher than those of SLSTR for high intensity fires (>4000 MW). It appears that the outlier fire is the result of a large quantity of small-fire detections by SLSTR leading to the formation of a very large supercluster, comprised of a majority of commissioned pixels. The very large FRP difference is the consequence of the clustering methodology and a very high number of low-intensity commissions in the same area.

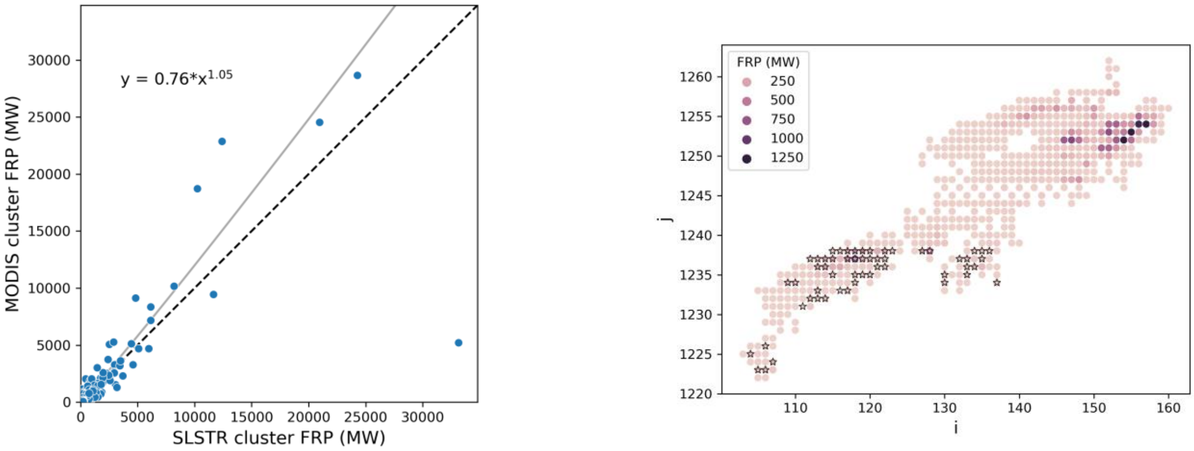

Figure 40: On the left, comparison between the FRP of cluster pairs detected by SLSTR and MODIS during daytime. The outlier on the bottom right has been removed when performing the power-law fit. On the right, the outlier supercluster displayed in image grid coordinates. The circles are the fires detected by SLSTR, the stars those detected by MODIS. The hue indicates the FRP estimated for each fire.

7.3.4 Biome influence on active fire detection

The present section consists in a preliminary study on the biome influence over errors of commission and omission. The biome corresponding to each fire is determined using the Global Land Cover 2000 data. This per-biome analysis may help identify biome-dependent behaviours concerning active fire detection. For each biome, over nighttime and daytime, the absolute numbers of commissions and omissions as well as the relative numbers (with regards to the total number of SLSTR and MODIS AFP for commissions and omissions, respectively) are evaluated over the April—June 2023 period.

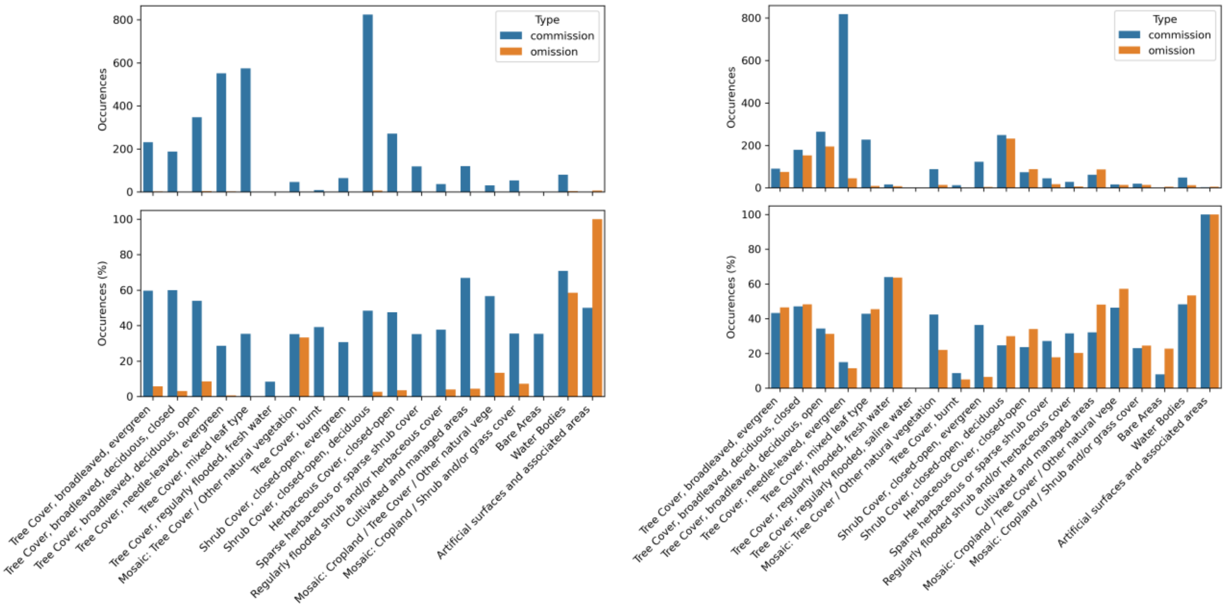

Figure 41: Occurrences of commissions and omissions of active fire pixels per biome. On the left, nighttime; on the right, daytime.

Figure 41 shows the absolute and relative number of commissions and omissions. For both nighttime and daytime, the four biomes with the most commissions are: Treed Open Broadleaved Deciduous, Treed Needle-leaved Evergreen, Treed Mixed Leaf Type, and Shrubland Closed-Open Deciduous. However, as a proportion of the total number of AFP detected by SLSTR, the percentage of commissions from Treed Needle-leaved Evergreen is much lower than the average, with values below 30% and 20% versus 49% and 31% for nighttime and daytime, respectively. In general, the three Treed Broadleaved biomes (Evergreen, Deciduous Open, Deciduous Closed) all have higher than average percentages of commissions with non-negligible quantities of active fire detections.

7.4 Conclusion

The first result from this performance report is that the accuracy improvements of the geographic locations of fires in the FRP monitoring algorithm seem to have led to a reduction in the number of commissions and omissions compared to previous periods. Trends in future analyses may confirm this. Nevertheless, for this period, the active fires detected by the satellites were much more in line, with increased numbers of double detections.

Overall, in line with previous reports, it appears that for both nighttime and daytime products, much more AFP are detected by SLSTR than MODIS. Indeed, SLSTR’s FRP threshold to detect active fires is much lower than that of MODIS (<1 MW vs 3 MW), leading to a very high number of low intensity commissioned fires. On the other hand, the tail of the FRP retrieved by MODIS over the April—June 2023 period was much longer than the one of SLSTR. It appears that the maximum FRP estimated from SLSTR can be much lower than the ones estimated from MODIS. This pattern is true for both night and daytime.

For most active fire clusters, trends are coherent with past periods, with good agreement between SLSTR and MODIS clusters’ FRP. However, the very high intensity fires over the current period have allowed to see that for very high intensity fire clusters (>4000 MW), SLSTR usually leads to lower FRP values than MODIS. The scaling factor is not linear and seems akin to a power-law. Further work is required to better understand whether this is a general finding or the result of a one-time event.

The first results of the per-biome analysis seem to show behavioural differences between Broadleaved and Needle-leaved biomes: although both present high quantities of fire detections, as would be expected from forests, the former are much more prone to commissions than the latter (>55% versus <30% and >33% versus <15%, for nighttime and daytime, respectively). Although they have a percentage of commissions lower than the average, Shrublands Closed-Open Deciduous presented a very high quantity of commissions at nighttime. Future reports will help identify trends and potential explanations regarding the distribution of omissions and commissions per biome.

8 Appendix A

All Data Quality Reports, as well as past years Data Quality Reports and Annual Performance Reports, are available on dedicated pages in Sentinel Online website, at:

- https://sentinel.esa.int/web/sentinel/technical-guides/sentinel-2-msi/data-quality-reports
- https://sentinel.esa.int/web/sentinel/technical-guides/sentinel-3-olci/data-quality-reports
- https://sentinel.esa.int/web/sentinel/technical-guides/sentinel-3-slstr/data-quality-reports
- OPT Annual Performance Report Year 2022 (PDF document)

End of document